$^{12}C(\alpha,\gamma)^{16}O$ Reaction at Low Energies

Thesis by

Richard M. Kremer

In Partial Fulfillment of the Requirements

for the Degree of

Doctor of Philosophy

California Institute of Technology

Pasadena, California

1987

(Submitted May 26 1987)

Acknowledgments

There are many people whose help has been invaluable in undertaking this project, but first and foremost, I want to thank my wife for her constant support and for bearing our children who are the joy of my life.

I want to thank Dr. Brad Filippone whose efforts on this experiment were, and continue to be, superhuman. His enthusiasm for physics and his strict adherence to the principles of the scientific method will be a guide for me the rest of my life.

I want to thank Dr. Charles Barnes, whose sincerity, honesty, and support led to a truly unbiased result.

Also, I would like to thank Dr. Leon Mitchell, Dr. Hugh Evans, and Dr. Kai Chang whose participation in the long runs on the accelerator and whose help in interpreting the data made this project possible.

Finally, I would like to thank the students of Ruddock House for injecting periods of forced responsibility into my life, reminding me that the real world lurks just off-campus.

ABSTRACT

Absolute total cross-sections for ground state, $^{12}C(\alpha,\gamma_0)^{16}O$ and cascade, $^{12}C(\alpha,\gamma_C)^{16}O$, transitions were measured over the energy range 1.29 MeV to 3.29 MeV. γ-rays were detected with four large NaI(Tl) crystals in close geometry around a ^{4}He gas target. Recoil ^{16}O ions were separated from the intense ^{12}C beam and detected by a multiwire proportional and gas ionization chambers in time-of-flight delayed coincidence with the γ-rays. The total cross-section at the peak of the E_{cm} = 2.4 MeV, $J^{\pi} = 1^{-}$ resonance was found to be 42.6 ± 3.6 nb and the extrapolated S-factor at 300 keV was determined to be 40^{+40}_{-34} keV-barns.

Table of Contents

Table of Contents, Continued

List of Figures

I. INTRODUCTION:

When the proton fuel in the core of an intermediate mass star is exhausted, hydrogen burning continues in an expanding spherical shell. At this stage, the core of the star is no longer supported by the thermal pressure generated by nuclear reactions and gravitational collapse begins. The core contracts until sufficient gravitational energy is converted to thermal energy, and the density becomes high enough to ignite helium burning, the first step of which is $3\alpha \rightarrow {}^{12}C$. This triple-alpha process bridges the mass five and eight instability gaps and initiates the nucleosynthesis of elements with A > 12. The rate of this reaction at stellar energies is known to about 15% from previous work. (BA80,F083)

Carbon from the triple-alpha process is consumed by the ${}^{12}C(\alpha,\gamma){}^{16}O$ reaction. Since the possible ${}^{16}O$ consuming reaction, ${}^{16}O(\alpha,\gamma){}^{20}Ne$, is expected to be slow (F083) at stellar energies the relative rates of ${}^{12}C(\alpha,\gamma){}^{16}O$ and $3\alpha \rightarrow {}^{12}C$ reactions effectively determine the relative abundances of ${}^{12}C$ and ${}^{16}O$ at the end of helium burning. Many of the conclusions about the subsequent evolutionary path of the star depend critically on the ${}^{12}C/{}^{16}O$ ratio (BA80,W086) present at the end of helium burning.

The relative abundances of all species in the mass range A = 12 to 60 produced by nuclear burning inside a star depend upon the carbon/oxygen ratio of the core of the star at the end of helium burning (W086). The star contracts and heats up until the next stage of nuclear burning is ignited. If ${}^{12}C$ is the predominant constituent in the core

then carbon burning is the next stage, which produces large amounts of ^{20}Ne and ^{24}Mg. However, if ^{16}O is the major ingredient, oxygen burning produces large amounts of ^{28}Si and ^{32}S, while making very little neon and magnesium. These different nucleosynthetic routes result in significantly different relative abundances for all elements below the peak of the nuclear binding energy maximum at A $\simeq$ 60 (BA80,WO86).

The size of the iron core at the end of quasistatic nuclear burning is what most sensitively determines the final evolutionary state of the star, whether it is to be a black hole or neutron star. As discussed above, the $^{12}C(\alpha,\gamma)^{16}O$ reaction rate effectively determines whether oxygen or carbon burning follows helium burning. Oxygen burning results in a much larger iron core than carbon burning. Therefore, if oxygen rather than carbon burning is the next important stage of the nucleosynthetic process, black holes may result from smaller mass stars than previously thought (WO86). The rate of the $^{12}C(\alpha,\gamma)^{16}O$ reaction thus plays a key role in our understanding of elemental synthesis and supernova dynamics.

At stellar energies the $^{12}C(\alpha,\gamma)^{16}O$ is expected to proceed by resonant capture from ℓ = 1 and ℓ = 2 partial waves followed by γ-decay to the ground or other bound states. When the γ decay proceeds directly to the ground state the ℓ = 1 partial wave results in an electric dipole (E1) transition while the ℓ = 2 partial wave gives an elecrtic quadrupole (E2) transition. When the γ decay goes through one of the bound states, either partial wave may result in E1, E2, M1, or M2 transitions depending upon the bound state selected. Electric dipole γ-decays are forbidden by the isospin selection rules which state that

no electric dipole transition may proceed by a $\Delta T = 0$ channel. All the states in ^{16}O below $E_x \sim 12$ MeV are $T = 0$, hence every transition is automatically $\Delta T = 0$. T^2 is a constant of the motion only to the extent that the nuclear forces involved are much more important than the coulomb forces. The coulomb forces break the symmetry and allow $\Delta T = 0$ dipole transitions.

A partial level diagram of ^{16}O, in which only the states relevant to $^{12}C(\alpha,\gamma)^{16}O$ are included, is shown in Figure 1. Of particular interest are the $J^\pi = 1^-$ states at $E_x = 7.12$ MeV and 9.59 MeV and the $J^\pi = 2^+$ state at $E_x = 6.92$ MeV. The capture cross-section at $E_{cm} = 300$ keV is expected to be dominated by the high energy tails of the subthreshold 1^- and 2^+ states.

The α-widths of these states cannot be measured directly since they are below the threshold to break up into α-particles.

The α-width of the $E_x = 7.12$ MeV, $J^\pi = 1^-$ state can be indirectly determined by observing the interference between this state and the $E_x = 9.59$ MeV, $J^\pi = 1^-$ state. The 9.59 MeV state is very broad ($\Gamma_{cm} = 500$ keV) and has sizable effects even at very low energies. Detailed measurements of the shape of this resonance, both above and below the peak, show deviations from the shape expected for a single isolated resonance. The deviations are partially due to interference with the sub-threshold $J^\pi = 1^-$ state, and this interference provides information on the width of the sub-threshold state.

The α-width of the sub-threshold $J^\pi = 2^+$ state can be determined by measurements of the angular distribution of γ-rays as a function of

energy. E2 radiation, for a zero incident spin channel, has a $\sin^2\theta \cos^2\theta$ dependence on the polar angle, while the E1 radiation has a $\sin^2\theta$ pattern. Detailed angular distribution measurements give the ratio of the E2 component to the E1 component.

The present experiment measures the interference between the $J^\pi = 1^-$ states by measuring the E1 cross-section to as low in energy as technically feasible which allows an extrapolation of the cross-section to stellar energies.

The rate of $^{12}C(\alpha,\gamma)^{16}O$ at stellar energies is poorly known. The only three measurements at low enough energies to be of interest disagree at the critical low energies.

Dyer and Barnes (DY74) used an α-particle beam incident upon an enriched ^{12}C target and observed the γ-rays. The enrichment of the target is important because of the neutron background from $^{13}C(\alpha,n)^{16}O$ caused by natural ^{13}C in the target. Even with ^{12}C enrichment, a bunched-chopped beam and time-of-flight techniques were required to distinguish the reaction γ-rays from the prompt neutrons which produce background in the detectors.

Kettner et al. (KE82) turned the reaction around and used a ^{4}He gas target and a ^{12}C beam and observed the γ-ray yield. This technique eliminates the ^{13}C contamination problem, but the measurement is still plagued by high γ-ray background from beam induced reactions, cosmic rays, and pile-up of γ-rays from natural radioactivity.

Redder et al. (RE85,RE87) used an intense α-particle beam and an

enriched ^{12}C target. They did not use time-of-flight to separate the γ-rays from the prompt neutrons, but they did employ germanium solid-state detectors. The Ge(Li) detectors have very good energy resolution so the number of background events that must be included in the γ-ray energy window is much less than for the NaI(Tl) detectors of the previous measurements. This experiment included extensive angular distribution measurements which distinguish between the E1 and E2 components.

The determination of the yield from $^{12}C(\alpha,\gamma)^{16}O$ below ~ 2 MeV requires a measurement of cross-sections smaller than one nanobarn, so it is clear that a technique coupling high detection efficiency and low background is necessary to improve substantially on the existing data.

In the present measurement, both the γ-ray and the recoil ^{16}O ions are detected in coincidence, thus enormously reducing problems from high background rates. A helium gas target and ^{12}C beam are used.

The γ-rays are detected with high efficiency NaI(Tl) detectors in close geometry around the target, and the recoil ^{16}O ions (projected forward by conservation of momentum) pass through a recoil separator to remove the main beam and are finally imaged upon a heavy ion detector.

This technique thus provides an essentially unambiguous signature of the $^{12}C(\alpha,\gamma)^{16}O$ reaction.

II. Experimental Apparatus and Method:

II-A. Target:

A windowless differentially pumped transmission gas target designed to transmit all ^{16}O recoils, shown schematically in Figure 2, was constructed for this measurement. It consists of five chambers, each isolated by a system of canals and apertures. Chamber 1 is the gas cell itself, which is 5.72 cm long and is shown in detail in Figure 3. Gas is fed in through a needle valve on the injection line at the top and exits through the 4.0 mm entrance aperture and the 6.0 mm exit aperture. Below and at 60^{o} to the beam direction, there is a silicon surface barrier (SI) detector which is used to monitor elastically scattered α-particles from a small section of the beam path in the target cell.

Chamber 2 completely surrounds chamber 1 and consists of a 10.2 cm diameter stainless steel pipe which is pumped by a model R1600 Leybold-Heraeus Roots blower. It is separated from chamber 3 (up-beam) by a 4.8 mm diameter by 96.5 mm long aluminum canal. Chamber 2 is separated from chamber 4 (down-beam) by a tapered and threaded 40 mm long aluminum exit canal. This canal is 3.5 mm diameter at the small (entrance) end and has a taper of 2^{o}. The inside surface of this canal is threaded to reduce the surface area that might forward scatter beam particles.

Chamber 3 is pumped by a model 3133C Sargent-Welch turbo-molecular pump and is separated from the accelerator beamline vacuum by a 23 cm long by 1 cm diameter stainless steel canal.

Chamber 4 is pumped by a model R150 Leybold-Heraeus Roots blower. Chambers 4 and 5 are separated by a 1 cm diameter aluminum aperture.

Chamber 5 is pumped by a model 3133C Sargent-Welch turbo-molecular pump and is separated from the recoil separator by a 5 cm diameter by 7.6 cm long canal.

During data runs, with the target pressure at 2.50 torr, typical pressures in the chambers are:

Beam Line	2×10^{-7} Torr
Chamber 1	2.50 torr
Chamber 2	0.2 Torr
Chamber 3	2×10^{-5} Torr
Chamber 4	4×10^{-2} Torr
Chamber 5	1×10^{-4} Torr
Recoil Separator	2×10^{-5} Torr

The target pressure is monitored with a model 222B M.K.S. Baratron with resolution of 0.01 torr. Elsewhere in the system, pressures are monitored by thermocouple and ionization gauges.

II-B. Detection Apparatus:

The essential difference between this experiment and previous work is that both product particles, the γ-ray and the ^{16}O nucleus, are detected in Time-of-Flight coincidence, and the energy and rate of energy loss of the ^{16}O ion are measured. This provides a very clean signature of the

reaction.

II-B1. γ-Ray Detectors:

NaI(Tl) crystal scintillators are used for γ-ray detection because of their properties of good energy resolution, fast timing, and high detection efficiency. Four 15.2 cm x 15.2 cm x 25.4 cm rectangular crystals with 12.7 cm 10-stage phototubes were purchased from Bicron Corporation for this work. The crystals were arranged in close geometry to the target, as shown in Figure 4. The crystals have their long axis parallel to the beam axis and were placed so that the target is at the center of this axis. The one exception to this is the bottom left crystal which is translated up-beam 4.1 cm to make room for the pumping manifold for chamber 4.

Cosmic ray events in the NaI(Tl) detectors were vetoed by 1.3 cm thick plastic scintillators that cover the crystal array on the top and three sides. The phototubes for the NaI(Tl) detectors emerge on the fourth side, although the plastic scintillators extend to give partial veto shielding to that side as well.

The detector array is surrounded by 5 cm to 10 cm of lead shielding to reduce the room background rate. As in the case of the plastic scintillators, the lead shielding does not fully cover the up-beam side of the crystal array.

All of the above mentioned elements are stacked on roller bearings. The two halves of the detector and shielding assembly are withdrawn by

means of a steel lead screw for easy access to the target chamber and for accurate repositioning of the detector array after servicing the target chamber.

The NaI(Tl) crystals provided both energy and timing signals. The energy signal is taken off the sixth dynode since the photomultiplier is not yet saturated at this stage. For further details see Figure 5. The energy resolution of the detector array was measured to be 9% for the 0.661 MeV γ-ray from ^{137}Cs. The timing signal is taken from the anode where the saturated pulse height results in less time slewing due to differences in pulse height. The timing resolution was measured to be 4.5 nsec for the ^{60}Co γ-ray cascade with a plastic scintillator start channel.

Due to the large size and close geometry of these crystals, the detection efficiency for γ-rays in the energy region of interest is $\geq$ 50%.

II-B2. Recoil Separator:

A recoil separator specifically designed to separate ^{16}O and ^{12}C of the same momentum was built for this experiment. The recoil separator is located at 0^{o} to accept all of the reaction ^{16}O. There are six active elements 1) a large aperture magnetic quadrupole doublet lens, 2) a Wien velocity filter followed by a 3^{o} electrostatic deflection, 3) a velocity defining slit, 4) a vertically converging quadrupole singlet lens, 5) a 60^{o} dipole sector magnet, and 6) a recoil particle detector. The arrangement and dimensions of the separator and its components are shown

in Figure 6.

The beam phase space due to these elements was calculated using the code TRANSPORT (BN77) and a Monte Carlo simulation of the initial conditions. The positions of the elements were optimized to maintain a small (< 3.5 cm) spot at the detector entrance. These simulations were used to guide the design of the recoil separator. An example of the first order optics calculations is shown in Figure 7.

After leaving the target, the ^{16}O ions have acquired a small transverse component of momentum from the emitted γ-ray. The quadrupole doublet accepts the diverging ^{16}O ions and brings them to a horizontal cross-over at the velocity slits. The Wien filter uses crossed **E** and **B** fields to balance the electric and magnetic forces on the charged particles which have the velocity of the recoil ^{16}O ions. The main ^{12}C beam, with a 33% higher velocity, is deflected by the Wien filter fields in this region. The Wien filter is the main beam rejection device in the system. The ^{16}O recoils are transmitted through the velocity slits and enter the quadrupole singlet. The quadrupole singlet and the dipole magnet together provide focusing for the recoil particles onto the detector. The three degree electrostatic deflection and the dipole magnet also separate the recoils from neutral components of the main beam.

The quadrupole doublet has a 10.2 cm aperture and is positioned as close to the target as possible. The distance from the center of the target to the beginning of the pole tips is 47.5 cm. If the quadrupole were even a few cm farther away, a significant fraction of the ^{16}O ions

would have diverged too far for the quadrupole magnet to focus them before they collide with the walls of the beam tube.

The velocity filter (Wien filter) consists of a vertical magnetic field and horizontal electric field (SA77). Charged particles must have velocity equal to cE/B to pass through this element undeflected. The magnet has rectangular pole tips 51 cm long and 17.5 cm wide. The pole tip gap is 9.5 cm. The electric plates are connected to ± 60 kV power supplies and the upper and lower edges are shaped (Figure 8) to make the field in the central region more uniform. Detailed calculations of the electric field distributions, using the code GUN (HE79), indicated a greater degree of uniformity using shaped rather than flat plates. The final design took into account ease of fabrication and delivery time. The effective length of the electric field is larger than that of the magnetic field, and extends beyond the magnetic field down-beam to impart a 3^{o} deflection to the ^{16}O recoils. This provides some rejection of the neutral particles in the main beam.

The velocity slit accepts only a small range of velocities near the selected velocity. It consists of two 1.3 cm thick water-cooled copper plates with stainless steel razor blades as the beam defining edges. Normally, the slit gap is 1.3 cm centered in the beam tube. The razor blades are used in an attempt to reduce forward scattering of the main beam. The slits accept velocities within approximately ± 1.5% of the selected velocity.

Following the velocity slit, the beam is diverging in both the vertical direction and in the horizontal direction. The beam is imaged

vertically by a vertically-converging, horizontally-diverging quadrupole singlet after the slits. The quadrupole singlet has a 7.6 cm aperture, and a maximum field at the pole tips of 2700 gauss.

The last focusing element is the 60^{o} dipole sector magnet. It provides horizontal focusing of the recoil ^{16}O onto the detector window as well as momentum selection for a final stage of beam rejection. The particles that are rejected at this stage are mainly neutrals and energy-degraded ^{12}C. This magnet has a 7.6 cm gap and a 32 cm radius of curvature. Fields as high as 13,000 gauss are obtainable.

For more background on this type of heavy ion separator, see the following references (CO81,HA81,EN81).

There are two vacuum pumps on the recoil separator: a 15.2 cm diameter oil diffusion pump located 1.60 meters down-beam from the target and a 20.3 cm diameter turbo-molecular pump 4.2 meters from the target. A 2.5 cm high and 7.6 cm wide pumping restriction is placed immediately up-beam from the Wien filter. The edges of the aperture are lined with razor blades to reduce the effects of scattered beam.

At 2.7 meters down-beam from the target, immediately after the Wien filter, another razor blade is positioned at the high velocity side of the Wien filter to intercept beam particles scattered off the Wien filter plates.

The beam dump (called the "Garbage Can") is 3.2 meters down beam from the target. It consists of a water-cooled tantalum cup. The cup itself is 7.6 cm tall and has a sharp edge to reduce scattering. It can

be moved perpendicular to the beam axis to optimize ^{12}C rejection and is designed to intercept the deflected ^{12}C beam only and so did not extend into the region of the beam pipe through which the ^{16}O passed.

There are two Faraday cups in the recoil system. One is directly above the turbo-molecular pump and the other is immediately in front of the detector. These helped in transporting the beam through the target and in determining the optimal recoil separator settings for each energy of beam.

II-B3. Recoil Particle Detector:

The recoil particle detector is the last element in the recoil separator. This detector generates three signals, timing, ΔE, and E.

The first signal is produced by a device in the first 2.5 cm of the detector which is called the timing detector. This is a multiwire proportional chamber that gives a fast rise time pulse to be used in the time-of-flight coincidence. The timing detector consists of three parallel grids of fine wires mounted perpendicular to the beam axis, following the design of Breskin (BR77). The two outside grids are held at ground potential and define the extent of the gas ionization that is important to the charge collection time. They are made of 20 μm gold-plated tungsten wires spaced 1.9 mm apart and are stretched over and epoxied onto a copper-coated fiberglas frame. The inner grid is supported in the same way as the outside grids but is made of 10 micron gold plated tungsten wires separated by 1.3 mm. The central grid is biased at +400 to +500 volts. The field in the region near the central

wires is intense enough to start a Geiger-type avalanche. The three grids are each separated by 3 mm so that the length of gas ionization sampled by this detector is 6 mm.

The timing detector occupies a region filled with 1.0 torr of isobutane. This region is separated from the vacuum of the recoil separator by a ~40 $\mu g/cm^2$, 3.8 cm diameter polypropylene window. In addition, the timing detector region is separated from the higher pressure in the EΔE detector by a similar window.

The timing resolution obtained with this detector is much better than that of the NaI(Tl) start channel. For 5.5 MeV alpha particles from ^{241}Am, a resolution of 1.9 ns was obtained with a silicon surface barrier detector stop channel. It has been shown (BR77) that for heavy ions, with their greater ionization per unit length, the timing resolution can be less than 1 ns.

The remaining chamber of the recoil detector produces the ΔE and E signals. The recoil particles enter the detector between a ground plane and a Frisch grid kept at +200 volts. Beyond the grid are the collector plates which are kept at +450 to +500 volts. The interior of the chamber is regulated at either 5.00 torr or 8.50 torr of isobutane depending upon the incident energy of the ^{16}O ions. The ions stop in the detector gas and produce a trail of ionization. The electrons produced in the ionization region drift through the grid and onto the collector plates. The amount of charge collected on each plate is proportional to the energy lost by the ion in the vicinity of the plate.

The first plate is 10.0 cm long and yields the ΔE signal. The

second plate is 27.7 cm long and provides the E signal. These two signals provide additional rejection of stray beam particles as ΔE and E will in general be different for background ^{12}C and the ^{16}O recoils.

The isobutane for this detector is constantly fed into the EΔE and timing regions, as shown in Figure 9. This constant gas flow prevents the gas from becoming contaminated by outgassing of the various materials used in the construction of this detector.

II-C. Beam Current Monitoring:

The gas target converts the charge state of the incident beam into an energy dependent distribution of charge states, making electrical charge collection an unreliable method of determining the number of beam particles. Therefore the beam particle intensity is monitored with a silicon surface barrier detector (SI detector) counting elastically scattered α-particles.

The active target area is much larger than the area viewed by the SI detector. The SI detector samples a small section of the beam near the center of the target chamber. A slotted aperture 2.5 mm wide and running transverse to the beam axis is located approximately 1.3 cm from the target center. A 0.5 mm pinhole located 6.3 cm from the beam axis is located immediately in front of the detector. The line defined by these apertures is at 60^{o} to the beam axis.

To produce a calibration for the SI detector a single cup calorimeter, which measures the beam power independently of the ion

charge state, was built. With the calorimeter mounted at the rear of a deep Faraday cup and the target gas removed, the calorimeter can be calibrated directly against the electrical beam current. Then, with gas in the target, the SI detector can be calibrated against the calorimeter as a function of energy.

The calorimeter itself, shown in Figure 10, was made following the design of Osborne (OS84). It is machined out of a single piece of copper, and the beamstop is connected to a heat-sink by a narrow cylinder of copper. The temperature at each end of the cylinder is measured with AD590 temperature transducers. These have the property that with a bias of between 5 and 30 volts they will pass a current in μamps equal to the Kelvin temperature. The time integrated temperature difference between the ends of the cylinder is proportional to the product of beam energy and the total number of beam particles. Osborne's calorimeter (OS84) was designed to measure beams up to 100 watts. The present calorimeter is designed for 1000 watts. A typical temperature difference across the cylinder during a data run is 20^{o} C.

II-D. Electronics:

The electronics set up for this measurement is shown in Figure 11.Eight pulse height signals are collected simultaneously whenever a coincidence is confirmed. These data included γ-ray energy from each NaI(Tl) detector, particle energy and energy loss, as well as timing information from the time-to-amplitude converter (TAC), and the timing detector pulse height. These data were passed to a CAMAC data

acquisition system interfaced to an LSI-11/23 for real time I/O and then data buffers were passed to the VAX 750 for on-line analysis and data storage on disk.

Two signals were taken from each NaI(Tl) crystal. The energy signals are shaped and amplified in a Timing-Filter-Amplifier (TFA) and then sent to one channel of an eight-channel Analog-to-Digital-Converter (ADC). The timing signals from the anode of each detector are passed through a discriminator and then through a fan-in to produce the (TAC) start signal. This signal also served as the strobe for the ADC to initiate conversion of the pulse heights into digital form. The ADC is automatically cleared after 15 μsec if no coincidence is detected.

The plastic scintillator cosmic-ray veto inhibits the ADC strobe whenever a coincidence is observed between events in the plastic and NaI(Tl) detectors. This reduces the background in the singles NaI(Tl) spectra by a factor of approximately 3 in the region $E_\gamma > 2.8$ MeV, but has a negligible effect on the efficiency for detection of reaction γ-rays.

The TAC stop pulse is provided by the timing detector. The signal is taken from the high voltage wires through an ORTEC 142A preamplifier. The energy "E" and timing "T" outputs are each fed into TFAs. The "T" output is then discriminated and used as the TAC stop. The "E" output is sent through a TFA and to the ADC so the pulse height can be obtained.

The particle energy (E) and energy-loss (ΔE) signals are preamplified and fed into spectroscopy amplifiers. The bipolar output signals are sent to the ADC for conversion.

Whenever the TAC has been started and stopped within its 2 μsec window, it generates a logic pulse as well as an analog pulse whose height is proportional to the time interval between the start and the stop signals. The analog pulse is the final input to the eight-channel ADC. The logic pulse blanks the ADC clear pulse and conversion continues to completion. All eight signals arrive within the strobe duration to be converted and tagged as one event. Typical singles rates in the NaI(Tl) detectors are 100 - 200 Hz, while singles rates in the timing detector are 5 - 30 kHz. The rate at which data are written event-by-event to the data acquisition computer is typically 2 - 20 Hz.

Independently, a pulse height spectrum from the SI detector is collected, giving the number of elastically scattered alpha-particles. Sometimes the rate in this detector is too high for our data collection system to handle easily, so the SI detector's 3511 ADC can be prescaled to accept only 10% or 1% of the true counts. In this way, the computer deadtime due to the SI detector ADC was typically <1%.

II-E. Accelerator and Ion Beams:

This experiment was carried out entirely at the NSF/CIT Pelletron Accelerator Facility located on the Caltech campus. The Pelletron is a 3 MV tandem accelerator with both external and internal ion source capability.

For most of the experiment, the ion source used was a General Ionex Cs sputter source. It produced beams of ^{12}C, ^{16}O, and protons. Typical beam currents at the entrance to the accelerator were;

^{12}C	60 μamps
^{16}O	30 μamps
p	5 μamps

Low energy (0.3 - 0.8 MeV) proton beams were produced in a RF ion source located in the accelerator terminal. These beams, used for calibration purposes, were typically ~ 100 namp.

^{12}C beams on target were typically 5 - 15 particle μamps. Other calibration beams were normally used at far lower intensities because of large reaction rates.

III. Data Analysis:

III-A. γ-Ray Detection Efficiency:

The NaI crystal detection efficiency is defined as the probability that a given γ-ray of energy E_γ will interact in the crystal array. In an environment completely free of background, this probability is merely the ratio of the number of γ-rays detected in the whole spectrum to the number produced at the source. This ratio may be determined in several ways.

The first of these is a calculation based on the method of Lazar et al. (LA56). This requires integration of the absorption over all possible γ-ray paths through the absorbing material between the source and the crystals and in the crystals themselves. This integral takes the form:

$$Eff=\iint_{cry} w(\Theta)\, e^{-\mu_a \ell_a(\Theta,\phi)} \left(1 - e^{-\mu_c \ell_c(\Theta,\phi)}\right) \sin\Theta \, d\Theta \, d\phi \quad (1)$$

where,

Θ = angle of γ-ray with respect to the beam axis.

ϕ = azimuthal angle of γ-ray with respect to some arbitrary x-axis.

μ_a = the mass attenuation coefficient for the absorbing material between the source and the crystal.

μ_c = the mass attenuation coefficient for γ-rays in NaI.

ℓ_a = the path length in the absorber that the γ-ray must pass through.

ℓ_c = the path length in the NaI crystals.

$w(\Theta)$ = The normalized angular distribution of the γ-rays.

In the present work the efficiency for both dipole (E1) and quadrupole (E2) radiation has been calculated. Figure 12 shows the results of this calculation for pure isotropic, pure dipole, and pure quadrupole radiation as a function of energy.

The efficiency can also be determined by measurements of an isotropic γ-ray distribution, such as the E_p = 340 keV, $J^\pi = 1^+$ resonance in the $^{19}F(p,\alpha\gamma)^{16}O$ reaction, in which there is an essentially one-to-one ratio of emitted α-particles to 6.13 MeV γ-rays. For this experiment a CaF_2 target is mounted at the center of the target cell. The α-particles are detected with a silicon surface barrier (SI) detector with precisely known geometric acceptance, while the γ-rays are detected by the NaI(Tl) crystals. The ratio of the counting rates in the two detectors is equal to the ratio of their respective efficiencies. Since the efficiency of the SI detector can be accurately determined from the geometry, the NaI(Tl) efficiency can therefore also be determined. The total efficiency of the NaI(Tl) detector array for 6.13 MeV γs was found to be 59.0 ± 3.0 % by this method.

The total efficiency can also be measured by using the E_p = 163 keV, $J^\pi = 2^+$ resonance in $^{11}B(p,\gamma)^{12}C$. In this reaction, ^{12}C is produced with 16.1 MeV of excitation energy and decays to the ground state via two channels. The ground state transition occurs 5% of the time and, the cascade through the 4.44 MeV state occurs 95% of the time (AJ85). The cascade gives a 4.44 MeV and an 11.66 MeV γ-ray which are independently analyzed. Data is taken with all four crystals on an event by event basis to allow offline analysis.

The efficiency for a single crystal is obtained by using three of the four crystals as monitor detectors and observing the coincident signals in the fourth crystal. A narrow window is placed on, say, the 11.7 MeV γ-ray in the monitor detectors, and the 4.4 MeV γ-ray is detected in the "live" detector. A background spectrum is produced by placing the cut at slightly higher channel numbers in the monitor spectra giving a spectrum from the "live" detector in coincidence with Compton tails of higher energy γ-rays as, well as accidental coincidences with cosmic-rays and room background pile up. The signal and background spectra are subtracted, and the total efficiency is just the number of nonzero pulse-height counts in the spectrum divided by the number of monitor signals obtained from the trigger crystals. This method works for both the 11.66 MeV and the 4.44 MeV γ-rays as monitor and determines the efficiency for the 4.44 MeV and 11.66 MeV γ-rays respectively. This procedure assumes that there is no angular correlation between the two γ-rays which is a good assumption to within 20% in this case.

The efficiency for pairs of crystals is obtained in a similar manner to that for single crystals. The only difference is that now two of the crystals have their digitized outputs summed prior to being histogrammed and only two crystals are available for the monitor. These spectra are produced for all possible combinations of pairs of crystals and single crystal monitors. This is different from the sum of the single crystal efficiencies because high energy γ-rays do not necessarily lose all of their energy in one crystal. Possible mechanisms include Compton scattering out of one crystal and into another and pair

production in which one of the 0.511 MeV quanta escape into another crystal.

Three-crystal efficiency is obtained in the same way. Three crystals are summed while the other crystal is used as monitor for each single crystal.

The efficiency for four crystals is obtained by plotting the efficiency per crystal determined above versus the number of crystals. The three points fall on a line which is extrapolated to four crystals. The total efficiency for four crystals for 4.44 MeV γ-rays is (56.6 ± 1.3)% and for 11.66 MeV γ-rays is (60.4 ± 0.9)%.

The variation of the efficiency with γ-ray energy is determined by interpolating between the three points found above.

The γ-ray efficiency discussed above is for a point source located at the center of the target chamber while the source of γ-rays for the experiment is extended over about 6 cm. The size of the correction for this effect is expected to be small. This effect can be calculated by repeatedly evaluating the integral in equation (1) with different positions for the point source evenly spaced along the z-axis and averaging over the answers. The validity of this calculation was checked by comparing the results with the measured relative efficiency for 9.1 MeV γ-rays from $^{13}C(p,\gamma)^{14}N$ for targets located at the front and center of the target chamber. The correction arising from the extended target reduces the efficiency from what it would be for a point source by 3-5% depending upon the incident energy.

III-B. NaI Spectrum Fraction:

For the ground state cross-section analysis only large pulse heights (E_C > 7.4 MeV) are accepted in the γ-ray spectra as valid events, thereby reducing the number of background events. It is then necessary to know the proportion of the NaI(Tl) pulse-height spectrum included in the γ-ray window. This fraction is called the Spectrum Fraction.

Background free γ-ray spectra can be obtained at 4.4 MeV and 11.7 MeV for 1, 2, and 3 crystals summed as described in the previous section. The spectrum fraction is just the number of events with pulse heights above E_C divided by the number of events in the entire spectrum. The spectrum fraction obtained is plotted versus the number of crystals summed and extrapolated to zero and to four crystals. The fraction extrapolated to zero crystals is the "Zero-Summing" spectrum fraction and the fraction extrapolated to four crystals is called the "Four-Crystal" spectrum fraction.

The "Four-Crystal" spectrum fraction can be independently measured using the $^{19}F(p,\alpha\gamma)^{16}O$ reaction which is a prodigious, isotropic source of 6.1 MeV γ-rays. A background-free spectrum for all four crystals summed is generated, since the signal swamps the background except at the lowest pulse heights. The spectrum fraction curves obtained for four crystals at 4.4, 6.1, and 11.7 MeV, using the two methods, are identical to less than 2% when the cutoff energy is scaled by the γ-ray energy.

The "Zero-Summing" curves at 4.4 and 11.7 MeV are also identical,

except for E_C/E_γ very close to 1 (see Figure 13). The fact that the "Four-Crystal" case was shown to be constant at an intermediate energy is evidence that the "Zero-Summing" case is constant as well.

The values used in this analysis were extracted from the curve for each energy for which data were taken and is plotted in Figure 14.

III-C. Efficiency of EΔE Detector:

Particles can be lost in transit between the target chamber and the detector. This type of loss arises mainly from the fact that the electromagnetic elements in the recoil separator must be tuned to pass only one charge state. All other charge states are not transported to the detector. The charge state fractions of the recoil particles are discussed later.

Recoil particle losses might also occur by collisions with canals, slits, apertures, or anti-scatter baffles. The placement and sizes of these beamline elements were guided by the Monte Carlo calculation of the recoil trajectories so that no loss due to beam divergence in the target chamber is expected, except at the lowest energies where as much as 5% of the beam could intersect the beam pipe through the large quadrupole doublet.

There might also be losses after a true stop signal has been received. Recall that the timing detector is in the up-beam chamber of the EΔE detector. The recoil particles can hit one of the wires in the

timing detector and produce a signal, but be absorbed so that no E or ΔE signal is produced. This effect was measured by directing a pilot beam of ^{16}O ions into the detector while gating the electronics on the timing detector, thus producing a spectrum of E and ΔE. The ratio of ions detected in the $E\Delta E$ peak to those detected in the channel corresponding to $E = 0$ and $\Delta E = 0$ was thus determined. It was found that 3.8% of the beam was lost in the timing detector which is consistent with the geometric cross-section of the wires. For these measurements, it is important to keep the rate in the detector below about 20 kHz to minimize effects due to summing out (pile up).

Summing out can also produce a small loss of signal in the $E\Delta E$ window. The high background rate of energy degraded ^{12}C beam particles can cause summing out of the recoils from the appropriate window. This effect was measured by directing the pilot beam of ^{16}O ions into the detector and taking runs at differing rates. The loss from summing out was found to be less than 5% for rates less than 30 kHz.

III-D. Calorimeter Calibration:

The calorimeter supplies a DC current in μamps equal to the Kelvin temperature difference between the beam-stop and the heat-sink. The temperature difference, ΔT, is proportional to the heat flux (power) passing from one end of the rod to the other. The time integrated power is proportional to the beam energy multiplied by the number of beam particles.

With the calorimeter mounted in a deep Faraday cup both the

electrical current and the temperature difference can be simultaneously integrated and the exact proportionality can be determined. The integrated temperature difference must be scaled by the incident beam energy just as the integrated electrical current must be scaled by the charge state of the incident beam. Then the number of beam particles measured in particle-μcoulombs becomes:

$$\text{beam} = \frac{1}{Q_o} \int i(t)\, dt = \frac{K}{E_b} \int \Delta T\, dt, \qquad (2)$$

where K is a proportionality constant, E_b is the beam energy, Q_o is the incident charge state of the calibration beam, and i(t) is the electrical current measured by the Faraday cup. The calibration constant was determined by using calibration beams of ^{12}C and ^{16}O with energies covering the entire energy range of this experiment. The result is: $K = 5.88 \pm 0.10$ MeV μcoul/(K^{o}sec).

III-E. Silicon Surface Barrier Detector Calibration:

The response of the SI detector to elastically scattered α-particles was calibrated against the calorimeter for several target pressures. Beams of ^{12}C and ^{16}O were directed through the target cell and onto the calorimeter. The number of α-particles detected by the SI detector is found to vary directly with the beam intensity and target pressure. The SI detector response is calibrated at each beam energy for which coincident data is taken. The SI detector calibration as a function of energy for ^{12}C beams is shown in Figure 15. The ^{12}C calibration was used

for determining the number of beam particles during the data runs. The ^{16}O calibration was used for determining the number of beam particles during the charge state fraction measurements.

III-F. Charge State Fraction:

The charge state fraction is defined as the ratio of the number of recoil ^{16}O ions emerging from the target in the selected charge state to the total number of recoil ^{16}O ions. The charge state fractions for an incident ^{16}O beam were measured at each energy by directing a pilot beam of ^{16}O with the same momentum as the bombarding ^{12}C beam through the gas target. The emerging beam was then analyzed by the recoil separator so that the selected charge state was incident on a Faraday cup immediately before the EΔE detector. The selected beam was electrically integrated at the detector cup while the SI detector simultaneously monitored the total ^{16}O beam dose. The charge state fraction is then the ratio of the number of ^{16}O ions of the charge state selected to the total number of beam particles. This was measured at each energy that was used for data collection, as well as for several target pressures (Figure 16). The variation in charge state fraction with pressure indicates that ~20% of the full target thickness is required to equilibrate the ^{16}O charge state distribution.

^{16}O ions produced in the last 20% of the target do not have a chance to fully equilibrate. It is unlikely that the initial charge state distribution of the reaction ^{16}O is the same as the initial charge

state distribution of the pilot ^{16}O beam, so the approach to equilibrium is different than that measured for the pilot beam. To test this effect the charge state fraction was measured as a function of target pressure. Target pressure was varied from 1.5 to 2.5 torr, and the $^{12}C(\alpha,\gamma)^{16}O$ reaction was run at the peak of the $J^{\pi} = 1^{-}$ resonance. The yield per μamp-torr will change, with changing pressure, commensurate with the change in charge state fraction for the selected charge state. The charge state fraction of the recoils in the 5^{+} state did not vary with pressure within the 15% statistical errors of this measurement. The value used for the charge state fraction in the analysis of the data are 95% of the values measured for the ^{16}O pilot beam, with the error estimated at 7%.

The rate of change with position in the target of the number of reaction ^{16}O ions in a given charge state is merely the number that are charge-exchanged into that charge state per unit target thickness minus the number that are charge-exchanged out of that charge state per unit target thickness plus the number that are created in that charge state per unit target thickness. That is:

$$\frac{dN_i}{dx}(E_b,\tau) = \sum_{j=0}^{8} N_j \sigma_{ji} (1 - \delta_{ij}) - \sum_{j=0}^{8} N_i \sigma_{ij} (1 - \delta_{ij}) + R_i \qquad (3)$$

Where σ_{ij} is the matrix of charge exchange probabilities from charge state i to charge state j taken from Macdonald and Martin (MA71). N_i is the number of ions in charge state i and R_i is the rate of production

of ^{16}O ions in charge state i.

From equation (3), a system of nine simultaneous differential equations is produced and is solved using a Runge-Kutta (C065) technique. The initial charge state of the recoil ^{16}O ions is unknown so the integration was done for a wide range of initial charge state distributions, recoil energies, and target thicknesses. A comparison is made between the calculated charge state fraction of the desired charge state using a 3.5 $\mu g/cm^2$ target and the calculated equilibrium charge state fraction given by using a 35.0 $\mu g/cm^2$ target for several recoil particle energies. The results indicated that the charge state distribution for the recoil particles lead to a 5% smaller fraction for the desired charge state than the fraction measured with the ^{16}O beam in equilibrium.

III-G. Target Thickness:

Accurate determination of the number of target atoms/cm^2 is necessary for the measurement of the total cross section. The target thickness was determined with a series of three measurements for this experiment. The first of these measurements employed the $^{16}O(\alpha,\gamma)^{20}Ne$, $J^{\pi} = 1^-$ resonance at E_x = 5.79 MeV. The excitation function for this resonance was measured using the calorimeter to measure the beam intensity. The width of the step in the excitation function is related to the target thickness and was fitted to a Breit-Wigner resonance shape as in Gove (G059). The width of this resonance (Γ_{cm} = 13 ev) is much less than the anticipated thickness of the target, so the full width at half maximum

of the step in the excitation function is equal to the energy loss in the target.

The same procedure was used to extract the target thickness from the $^{12}C(\alpha,\gamma)^{16}O$, $J^{\pi} = 2^{+}$ resonance at E_x = 9.847 MeV. The target is semi-thick to this resonance (Γ_{cm} = 0.625 keV), so the yield does not reach the thick target value and a fit to the Breit-Wigner shape is used to extract the target thickness. These data were fitted with the code FITIT (BE69). The step in the excitation function reaches 92.6% of the thick target yield at its highest point.

The target thickness was also measured by determining the energy loss of protons as they pass through the target gas. A 50 $\mu g/cm^2$ target of ^{27}Al was placed in a Faraday cup down-beam from the gas target cell. An excitation function of the strong E_p = 0.992 MeV resonance in $^{27}Al(p,\gamma)^{28}Si$ was produced both with gas in the target and without gas. The shift in the beam energy necessary to reach the half height of the thick target yield, for gas in compared with gas out, is the energy loss of the beam. Since we expect the energy loss of the proton beam in passing through the gas to be only about 1 keV and the tuning of the proton beam is difficult to reproduce at that level, the beam energy was changed by biasing the target with a 3kV variable battery. The target bias was measured before and after each run with a high-voltage-probe and digital voltmeter. The γ-ray yield was measured with a 3" x 3" NaI(Tl) detector placed near the target.

To convert each of these measurements of energy loss to the number of target particles per unit area, it is necessary to know the stopping

power of the various ions in ^{4}He gas. The stopping power was taken from the global fits of Ziegler & Anderson (AZ77,ZI80). Results of these three separate measurements are:

$^{12}C(\alpha,\gamma)^{16}O$	3.55 ± 0.19 $\mu g/cm^2$
$^{16}O(\alpha,\gamma)^{20}Ne$	3.57 ± 0.18 $\mu g/cm^2$
$^{27}Al(p,\gamma)^{28}Si$	3.64 ± 0.20 $\mu g/cm^2$

As the dominant error in the results above is due to the error in the stopping power taken from Ziegler and Anderson (AZ77,ZI80), the uncertainties on the above numbers are not completely independent. The value used for the target thickness is 3.58 ± 0.14 $\mu g/cm^2$. This value is consistent to within 10%, with the estimate resulting from multiplying the target pressure by the target length.

III-H. Target Profile:

The location and distribution of the target gas is relevant to the γ-ray efficiency calculations described earlier. The target pressure profile was measured using a silicon surface barrier detector at 90^{o} and detecting protons elastically scattered by the target material. The detector was collimated to view only a very small segment of the beam path and installed at five different places along the beam path; three positions inside the target cell (chamber 1 Figure 2) and one each in front and behind the target cell (chamber 2 Figure 2). As shown in Figure 17, the target density was constant to better than 2% in the

interior region of the target cell and fell to about 10% of that value outside. This is consistent with the pressure measurements in those regions.

III-I. Extraction of Yields:

The multiparameter data from this experiment can be presented in several ways. To best analyze the data so that the number of coincident events is most easily extracted, it is required that an event have E, ΔE, and E_γ values within certain limits, and then a time-of-flight (TAC) histogram is produced for these events. This has the main advantage that background counts occur randomly in time and hence give a flat background from which it is easy to extract yields.

The position of the peak in the TAC spectrum is clearly visible even for the lowest cross-section points, (signal/noise > 3) and scales inversely with the velocity of the ^{16}O recoil, as expected. The time dispersion due to slewing of the discriminator firing time for varying pulse heights or non-constant response of the other electronics is found to be negligible compared to the time dispersion from the kinematic Doppler broadening.

Any pulse height greater than ~1.3 MeV is accepted as a valid start in the NaI(Tl) crystals. Such a low cut allows the cascade radiation from the $J^\pi = 2^+$ and 4^+ resonances to be included in the γ-ray spectrum.

The positions of the E and ΔE cuts were determined prior to each

run by producing a low intensity ^{16}O (~1 kHz) beam of the same energy as the recoil ^{16}O and focusing it into the EΔE detector (these cuts can be reset off-line to check systematics). This low intensity beam, called the "screwball" beam, was produced as follows. First the Tandem accelerator was set to accelerate ^{16}O, ions and the analyzing magnet was set at exactly the NMR values to be used for data collection, thus imaging ^{16}O ions of the required charge state and momentum on the image slits. Second, the switching magnet was set to select ions with the same momentum, but with charge state +7. There are always some of these high charge state ions present due to stripping in the residual gas in the high vacuum line between the image slits and the switching magnet. This procedure greatly reduces the beam current entering the target chamber. Lastly, the "screwball" beam equilibrates in the target gas, and the selected charge state is imaged upon the recoil detector. The momentum dispersion of this beam will be less than the dispersion of the reaction ^{16}O ions because of the momentum imparted to the reaction ^{16}O ions by the γ-ray, but the central value of each is nearly the same. The validity of this method is checked by comparing the windows obtained to the windows extracted from high yield runs. In every case the centroid of the beam particles differed from the centroid of the reaction ^{16}O ions by less than 5% of the full width of the peak on either the E or ΔE axis. The appropriate widths were determined from the data runs rather than the ^{16}O beams because of the difference in dispersion.

During off-line analysis the data were replayed using the predetermined E, ΔE, and E_γ cuts, and a TAC spectrum was produced. The

number of coincidences was extracted from the TAC spectrum. Samples of the TAC spectra are shown in Figure 18.

The γ_0 signal, above the cutoff energy, (E_c = 7.4 MeV) is complicated by the summing of the cascade γ-rays which produce a signal similar to that from γ_0. The data must be extrapolated to 'zero summing' to remove the contribution from the cascade transitions.

The magnitude of this extrapolation is expected to be small for most of the data since the ground state reaction dominates, and the detection efficiency for the cascade γ-rays, above E_c = 7.4 MeV, goes as ε^2 (where ε is the single γ-ray detection efficiency) while the detection efficiency for the single ground state γ-ray goes as ε.

Only for the two highest energy data points does the cascade cross-section exceed the ground state cross-section. This is due to the influence of the strong $J^\pi = 4^+$ resonance at E_{cm} = 3.19 MeV which decays almost exclusively through the cascade channels (AJ86). For these data points the extrapolation is sizable.

In addition to the cuts on E and ΔE, the γ-ray window was set from 7.4 to 12.0 MeV. With these cuts, a TAC spectrum was produced for several NaI(Tl) detector summing schemes. First, a signal in the γ-ray energy window is required from exactly one detector for a valid coincidence. A separate TAC spectrum is produced with the crystal outputs summed in pairs. The same is done for crystal outputs summed in threes and fours for all possible combinations of 1, 2, 3, or 4 crystals. This has the effect of increasing the detector size without affecting the single γ-ray efficiency.

The TAC spectrum for, say, the 3-crystal case counts all of the events in the 2-crystal case plus any incremental yield due to events for which energy is collected in 3 detectors.

The usefulness of this method for extracting the γ_0 yield lies in the fact that the efficiency for detecting the single γ-ray is proportional to the number of crystals summed, whereas the efficiency for detecting the pair of cascade γ-rays goes as the square of the number of crystals summed. For a detailed explanation, see Appendix B.

The yield for each n-crystal case is divided by the appropriate single crystal γ-ray efficiency (normalized to 1.0 for 4 crystals summed) and plotted versus γ-ray efficiency. The result is a linear plot in which the intercept is the γ_0 yield in the absence of the γ_C signal.

Some of the γ_0 signal is lost by this method. Those γ_0 events for which the γ-ray Compton scatters in one crystal and deposits its remaining energy in a different crystal are also subtracted. To account for this effect, it is important to extrapolate the spectrum fraction curve to zero summing in exactly the same way.

III-J. Reaction Energy Determination:

The cross-section and S-factor vary rapidly with energy, thus it is important to accurately determine the effective reaction energy. The average energy at which the $^{12}C(\alpha,\gamma)^{16}O$ reactions occur is not equal to the incident beam energy. The beam particles lose energy in the target material, hence the reactions can happen over a range of energies. The

cross-section for the reaction is, in general, changing over this energy range. Therefore the appropriate average energy is weighted directly by the cross-section as a function of energy and inversely by the energy loss per unit target thickness. That is,

$$\bar{E} = \frac{\int_{E_i}^{E_i-\tau} dE\ E\ \sigma(E)\ (\frac{dE}{dx})^{-1}}{\int_{E_i}^{E_i-\tau} dE\ \sigma(E)\ (\frac{dE}{dx})^{-1}} , \qquad (4)$$

where $\sigma(E)$ is the cross-section, dE/dx is the energy loss per unit target thickness, and τ is the total energy loss in the target given by

$$\tau = \int_0^n (\frac{dE}{dx})\ dx , \qquad (5)$$

where n is the number of target atoms per unit area.

The above equations determine the average reaction energy for each run. However the calculation of the average energy requires a detailed knowledge of the energy dependence of the cross-section. A three-level R-matrix parameterization of the cross-section was used to determine the energy dependence. The R-matrix parameters were those of Weisser et al.(WE74).

In every case, the average energy determined in this way differed from that determined by the formula $\bar{E} = E_i - \tau/2$ (where τ is the energy loss of the ion in the target) by less than 2% of τ, because the target is thin compared to the rate of change of the cross-section with energy.

III-K. Transport Efficiencies:

The NaI(Tl) detectors have limited angular sensitivity and the recoil separator has a narrow momentum acceptance; these facts translate into different detection probabilities for the E1 and E2 reaction channels. The design of the recoil separator and the placement of the γ-ray detectors was determined by maximizing the detection efficiency for the E1, ground state reaction channel. It is important to know the transport efficiency for both the E1 and the E2 reactions.

The transport efficiency ($\varepsilon_{\gamma t}(E\ell)$) is defined as the probability that, for a particular multipole, the γ-ray will interact in the NaI(Tl) crystals, and the recoil ion of the desired charge state will be imaged onto the entrance window of the recoil detector. These two effects must be calculated together since they are coupled through the kinematics of the $^{12}C(\alpha,\gamma)^{16}O$ reaction. In less rigorous terms, the transport efficiency may be viewed as the probability of detecting the γ-ray and the recoil ion, in their respective detectors, given that one knows the multipolarity of the transition and the charge state of the ion.

The values of $\varepsilon_{\gamma t}(E\ell)$ were determined by a Monte Carlo calculation using the method of Lazar (LA56) for γ-ray detection efficiency and the code TRANSPORT (BN77) for recoil ion efficiency. The full range of initial conditions (radius and angle of dispersion), multiple scattering of the ^{12}C ion in the target gas before reacting, multiple scattering of the ^{16}O ion in the target gas after reacting, position in the target chamber where the reaction occurred, and the output angle of the γ-ray are all chosen randomly. One thousand iterations were done for each

energy, ℓ-value, and recoil ion charge state, so the intrinsic random error on this procedure is ~3%. The validity of this calculation was checked by comparing the results of calculation and measurement of the ratio of the yield from the E_{cm} = 2.68 MeV, $J^{\pi} = 2^{+}$ resonance in $^{12}C(\alpha,\gamma)^{16}O$ in coincidence to that obtained in singles mode operation. The experimental result was 0.49 ± 0.07, and the Monte Carlo calculation resulted in 0.45 ± 0.02.

Sensitivity of this system to ℓ-value comes mainly from velocity analysis through the Wien filter. Since the E2 γ-ray distribution is not peaked around $\theta = 90^{o}$ as is the E1, it results in a larger velocity dispersion than the E1 channel. The Wien filter converts this velocity dispersion into a spatial variation at the velocity slits. Therefore, a smaller fraction of ions from E2 reactions passes the velocity slits than from E1.

A smaller multipole dependence comes from the placement of the NaI(Tl) crystals. Due to the angular distribution of E1 and E2 radiation, the γ-ray detectors are about 15% more sensitive to E1 than to E2. The $\varepsilon_{\gamma t}(E\ell)$ values used for each data point in this experiment are displayed in Figure 19. The points shown are for ℓ = 1 and ℓ = 2 as well as for recoil ion charge states +3 and +5.

The angular acceptance of the recoil separator was measured by putting a calibrated ^{241}Am α-particle source 0.572 cm up-beam from the target chamber. This is the farthest up-beam that any significant number of recoil particles can be produced. The rate of α-particle detection divided by the rate of decays of the source is the fraction of the unit

sphere that is accepted by the recoil system. The result is 0.00267 Sr, which is larger than the required acceptance to transmit all the recoils of a given charge and momentum to the recoil detector.

The momentum acceptance of the system was measured using the $^{12}C(\alpha,\gamma)^{16}O$ reaction in the vicinity of the peak of the 1^- resonance at E_{cm} = 2.4 MeV. The beam energy was varied without changing the recoil separator settings, thus the number of detected events fell off as the recoil ion's momentum changed from the momentum set for the recoil separator. The momentum acceptance was found to be 3% FWHM.

For each energy the ideal separator settings were found by sending a low intensity "pilot" beam of ^{16}O ions through the system. This pilot beam had essentially the same velocity as the reaction recoils since the same analyzing magnet settings were used.

IV. Results And Conclusions:

IV-A. Ground State Cross-Section:

The $^{12}C(\alpha,\gamma_0)^{16}O$ yield curve was converted to cross-section using the formula:

$$\sigma_{\gamma_0}(E1) = \frac{Y\left(1 + \frac{\sigma_{E2}\,\varepsilon_{\gamma t}(E2)}{\sigma_{E1}\,\varepsilon_{\gamma t}(E1)}\right)^{-1}}{N_b\,\varepsilon_{cut}\,\varepsilon_{tim}\,\varepsilon_{spf}\,Q_f\,t\,\varepsilon_{\gamma t}(E1)} \qquad (6)$$

where,

Y = TAC yield with all data cuts in effect.

$\varepsilon_{\gamma t}(E\ell)$ γ_0/recoil transport efficiency for the appropriate multipole.

N_b = number of beam particles.

ε_{cuts} = efficiency of EΔE cuts.

ε_{tim} = efficiency of the timing detector.

ε_{spf} = γ-ray spectrum fraction with appropriate cuts.

$\sigma(E2)/\sigma(E1)$ = ratio of E2 to E1 cross-sections.

Q_f = charge state fraction

t = target thickness in particles/cm^2

The methods used to determine all of the above parameters are explained in the previous chapter, with the exception of $\sigma(E2)/\sigma(E1)$. The $\sigma(E2)/\sigma(E1)$ term merely accounts for the fact that a fraction of the observed yield comes from E2 rather than only E1. (For a derivation of the cross section formula see appendix D).

The ratio $\sigma(E2)/\sigma(E1)$ can be determined by measurements of the angular distribution of the $^{12}C(\alpha,\gamma)^{16}O$ reaction. The present experiment includes no such measurements so the $\sigma(E2)/\sigma(E1)$ ratio was taken from previous measurements and theoretical analysis of those measurements. The effects of the variations in the published values of $\sigma(E2)/\sigma(E1)$ on the cross-section ($\sigma_{\gamma_0}(E1)$) is not large compared to the experimental uncertainties as discussed below.

Three analyses (LA83,FU85,RE87) of $\sigma(E2)/\sigma(E1)$ as a function of energy were used in the extraction of $\sigma(E1)$. For comparison, the case where $\sigma(E2)/\sigma(E1) = 0$ at all energies was also done. The results of these calculations are:

Redder et al.'s $\sigma(E2)/\sigma(E1)$ → S(300 keV) = 46 keV-barns

Funck et al.'s $\sigma(E2)/\sigma(E1)$ → S(300 keV) = 20 keV-barns

Langanke & Koonin's $\sigma(E2)/\sigma(E1)$ → S(300 keV) = 40 keV-barns

$\sigma(E2)/\sigma(E1) = 0$ → S(300 keV) = 93 keV-barns.

The bulk of the analysis employed $\sigma(E2)/\sigma(E1)$ from Langanke and Koonin's theoretical fit to the data of Dyer and Barnes (DY74). Redder et al.'s (RE87) data are more complete than Dyer and Barnes' data and spans the energy range of all of our data points, but there is no theoretical analysis of this $\sigma(E2)/\sigma(E1)$ data as of this writing. Values were extracted from Redder et al.'s (RE87) data by drawing a smooth line through most of the data and reading the value from the graph. Funck et al.'s analysis was included since it showed the most rapid variation of $\sigma(E2)/\sigma(E1)$ in the stellar energy range. The $\sigma(E2)/\sigma(E1)$ ratios used for

each data point are shown in Figure 20.

Figure 21 shows the E1 cross-section for the ground state capture transition ($^{12}C(\alpha,\gamma_0)^{16}O$). The data are displayed in Table 1. The uncertainties in the data points are statistical plus a 5% random error arising from uncertainties in beam current normalization. These are the errors used in fitting the data and extrapolating to stellar energies.

IV-B. Cascade Cross-Section:

The cascade yield was extracted in the same way as the ground state transition yield. Since the data were extracted from a different portion of the same spectra as the ground state data, the ratio of the cascade cross section to the ground state cross section is given by the simple formula:

$$\frac{\sigma_{\gamma_C}}{\sigma_{\gamma_0}} = \frac{Y_{\gamma_C}\ \varepsilon_{spf}\ (\gamma_0)\ \varepsilon_{\gamma t}(\gamma_0)}{Y_{\gamma_0}\ \varepsilon_{spf}\ (\gamma_C)\ \varepsilon_{\gamma t}(\gamma_C)} \cdot \qquad (7)$$

Y_{γ_C} is the number of counts in the TAC spectrum with γ-ray energy window E_γ = 5.0 to 7.3 MeV minus the number of γ_0 counts expected in the TAC spectrum for that window. There are γ_0 counts in the γ-ray energy window E_γ = 5.0 to 7.3 MeV due to the Compton tail of the γ_0 pulse height spectrum. $\varepsilon_{\gamma t}(\gamma_C)$ is the transport efficiency given cascade γ-rays in an isotropic distribution. All other parameters are as

previously defined. A graph of this quantity is shown in Figure 22. Note that even the most pessimistic linear extrapolation of this ratio to stellar energy implies that the contribution from the cascade is less than 10%.

IV-C 2^+ Resonance Strength:

The strength of the narrow $J^\pi = 2^+$ resonance at $E_x = 9.85$ MeV in $^{12}C(\alpha,\gamma)^{16}O$ is one of the best known features of this reaction within the experimental energy range. Thus, a measurement of the strength of this resonance serves as a bench mark for the accuracy and validity of the experimental methods and techniques.

Coincident data were taken at the peak of the resonance and the γ_0 yield was extracted. This resonance is much stronger than the broad 1^- resonance in which it is embedded, therefore the γ-rays have a nearly pure E2 (quadrupole) distribution.

Using the fact that the target provided 92.6% of a thick target yield (Figure 23), the cross-section and Γ_{γ_0} could be calculated making use of the analysis of Sargood (SA82).

The result obtained was $\Gamma_{\gamma_0} = 5.5 \pm 0.7$ meV. This should be compared to the published value $\Gamma_{\gamma_0} = 5.7 \pm 0.6$ meV (AJ86).

IV-D. S-Factor:

The astrophysical S-factor is defined by the equation:

$$\sigma(E) = \frac{S(E)}{E} e^{-2\pi\eta} \qquad (8)$$

where $\eta = 2\pi Z_1 Z_2 e^2/\hbar v$. This is useful since the Coulomb penetrability contribution to the cross-section is divided out, leaving the slowly varying nuclear effects concentrated in the S-factor. The E1 S-factor derived from these measurements is shown in Figure 24 and listed in Table 2.

The agreement between this and previous measurements is reasonably good, although there are important differences. Most notably, the width of the $E_{cm} = 2.39$ resonance is generally narrower than widths established with elastic scattering data (PL87,J062,CL68). Redder et al. (RE87) and Dyer and Barnes (DY74) used the value of Γ_{2_α} from elastic scattering data in their fits to the $^{12}C(\alpha,\gamma)^{16}O$ data. Figure 25 shows the comparison between the present measurement and extrapolation with the data of Dyer and Barnes (DY74) and the data of Redder et al. (RE87).

IV-E. R-Matrix Analysis:

The E1 data were fitted using a 3-level R-matrix analysis. The R-matrix formalism is, in principle, exact if a complete set of basis states is used. In practice, restricting the basis to three states has been found

to be both expedient and satisfactory for the analysis of $^{12}C(\alpha,\gamma)^{16}O$ (WE74,RE87).

The R-Matrix formalism was developed following Weisser et al. (WE74). The cross-section is

$$\sigma = \frac{3\pi}{k^2} |U_{\alpha\gamma}|^2 \qquad (9)$$

where $hk/2\pi$ is the relative momentum of the α-particle and the ^{12}C and

$$U_{\alpha\gamma} = \sum_{\lambda,\lambda'=1}^{3} \Gamma_{\lambda\alpha}^{\frac{1}{2}} A_{\lambda\lambda'} \Gamma_{\lambda'\gamma}^{\frac{1}{2}}. \qquad (10)$$

The symbols $\Gamma_{\lambda\alpha}$ and $\Gamma_{\lambda\gamma}$ represent the α- and γ-widths respectively of the three levels. The level matrix $A_{\lambda\lambda'}$ is defined by

$$(A^{-1})_{\lambda\lambda'} = (E_\lambda - E)\ \delta_{\lambda\lambda'} + \Delta_{\lambda\lambda'} - \frac{i}{2} \Gamma_{\lambda\alpha}^{\frac{1}{2}} \Gamma_{\lambda'\alpha}^{\frac{1}{2}} \qquad (11)$$

where E_λ is the energy eigen-value of level λ, and E is the cm energy in the $^{12}C + \alpha$ system. The level shift matrix is

$$\Delta_{\lambda\lambda'} = -(S_\alpha^1 - B)\ \gamma_{\lambda\alpha}\ \gamma_{\lambda'\alpha}\ . \qquad (12)$$

Here $\gamma_{\lambda\alpha}^2$ is the reduced α-width of level λ defined by

$$\Gamma_{\lambda\alpha} = (2P_\alpha^1)\ \gamma_{\lambda\alpha}^2\ , \qquad (13)$$

and S_α^1 and P_α^1 are the $\ell = 1$ shift and penetrability functions. The

reduced γ-width is defined by

$$\Gamma_{\lambda\gamma}(E) = \left(\frac{Q+E}{Q+E_\lambda} \right)^3 \gamma^2_{\lambda\gamma} \qquad (14)$$

where Q = 7.161 MeV is the Q-value for the $^{12}C(\alpha,\gamma)^{16}O$ reaction.

The value of E_1 can be chosen (WE74) in such a way that the resonance term in the 3-level phase shift formula is $\pi/2$ at $E = E_b = -45$ keV, the cm energy of the $E_x = 7.12$ MeV bound state. This requires,

$$\left(\sum_\lambda \frac{\gamma^2_{\lambda\alpha}}{E_\lambda - E_b} \right)^{-1} - S^1_\alpha(E_b) + B = 0 \; . \qquad (15)$$

The value of the γ-width of the 7.12 MeV state used is $\Gamma_\gamma = 55$ meV (AJ86). The R-matrix expansion can be written as

$$\Gamma^{\frac{1}{2}}_\gamma(7.12) = \left(\sum_{\lambda'} \frac{\gamma^2_{\lambda'\alpha}}{(E_{\lambda'} - E_b)^2} \right)^{-\frac{1}{2}} \sum_\lambda \frac{\gamma_{\lambda\alpha}\, \Gamma^{\frac{1}{2}}_{\lambda\gamma}(E_b)}{E_\lambda - E_b} \; . \qquad (16)$$

Equation (14) and (16) can be solved for $\gamma_{1\gamma}$ in terms of the remaining parameters and the measured value of $\Gamma^{\frac{1}{2}}_\gamma(7.12)$.

The three states selected for the analysis are the $J^\pi = 1^-$ states at $E_{cm} = -0.045$ MeV (the 7.12 MeV bound state) and 2.39 MeV and a fictitious state at $E_{cm} = 13$ MeV.

The $E_{cm} = -0.045$ MeV and $E_{cm} = 2.39$ MeV states are the nearest $J^\pi = 1^-$ states to the stellar energy region, and the interference between these states effectively determines the reaction cross-section. The fictitious 13 MeV state is included to account for contributions

from high lying states and to prevent all observed interference effects from being ascribed to the sub-threshold state by default. To the extent that this third level approximates the effects of all high lying $J^{\pi} = 1^{-}$ states, this analysis will faithfully represent the cross-section in the stellar energy region. In the following, these states will be referred to by the numbers 1, 2, and 3 in order of ascending energy.

This formalism requires choosing, a priori, two parameters: the boundary parameter B and the interaction radius R. The quality of the fit to the data and the extrapolated values are largely independent of the exact values of R and B (WE74,LA58,DY74). R is chosen to be 5.5 fm which is approximately the expected sum of the radii of ^{12}C and ^{4}He. B was chosen so that the level-shift matrix (Δ_{ij}) is zero at the energy of the #2 resonance. This requires that B equal the shift function at E_{cm} = 2.39 MeV, i.e. B = -1.52. This choice of B reduces the coupling between the parameters of the #1 and #3 resonances.

Completing the R-Matrix parameterization, three parameters must be determined for each level. These are the resonance energy eigen-value (E_{λ}), the reduced γ-width ($\gamma_{\lambda\gamma}$), and the reduced α-width ($\gamma_{\lambda\alpha}$). The resonance energy of the #1 resonance is well known (AJ86). The energy eigen-value can be determined from the resonance energy, the boundary value B, and $\gamma_{\lambda\alpha}$ as described by Weisser et al.(WE74).

Since the level shift matrix is zero at E_2, the energy eigenvalue is equal to the resonance energy. The value E_2 = 2.39 MeV was used.

The eigen energy of the #3 state is not well defined. Elastic scattering data have been fitted with a 3-level R-matrix analysis with

values of E_3 ranging from 13 to 30 MeV (J062,CL68,PL87). Trial fits to the present data were generated with E_3 = 13, 20, and 30 MeV. No significant change in χ^2 was observed. The value E_3 = 13 MeV was chosen for this analysis following Weisser et al. (WE74) since the exact value does not appear to be critical.

Again, following Weisser et al., the value for γ_{3_α} was taken from the elastic scattering data. The value was that appropriate for the choice of E_3, i.e. γ_{3_α}= 1.80 $MeV^{\frac{1}{2}}$.

The four remaining parameters, γ_{1_α}, γ_{2_α}, γ_{2_γ}, and γ_{3_γ} are obtained from a fit to the S-factor data. Previous fits to $^{12}C(\alpha,\gamma)^{16}O$ data by Dyer & Barnes and Redder et al. have used only 3 floating parameters after adopting γ_{2_α} = 0.774 $MeV^{\frac{1}{2}}$ from elastic scattering data. As noted earlier, the width of the #2 resonance is narrower than the previous measurements.

There are three types of parameters used in this fit: fixed, variable (or floating), and calculated. An example of a fixed parameter is E_3 = 13 MeV. It does not change, and its value was selected a priori. There are four variable parameters which are selected to minimize χ^2 of the fit. The calculated parameters are E_1 (found by solving equation 15) and γ_{1_γ} (found by solving equations 14 and 16) which are determined from previous measurements and the values of the fixed and floating parameters.

The fixed parameters are,

γ_{3_α} = 1.80 $MeV^{\frac{1}{2}}$

R = 5.5 fm

B = -1.521

$\Gamma_\gamma(7.12)$ = 55 meV

E_b = -0.045 MeV

E_3 = 13.0 MeV

E_2 = 2.39 MeV.

The best fit floating parameters are,

$\gamma_{1_\alpha} = 0.19 \pm 0.03$ $MeV^{\frac{1}{2}}$

$\gamma_{2_\alpha} = 0.65 \pm 0.02$ $MeV^{\frac{1}{2}}$

$\gamma_{2_\gamma} = (-1.33 \pm 0.03) \times 10^{-4}$ $MeV^{\frac{1}{2}}$

$\gamma_{3_\gamma} = (-107 \pm 11) \times 10^{-5}$ $MeV^{\frac{1}{2}}$.

Finally the calculated parameters are,

E_1 = -0.088 MeV

$\gamma_{1_\gamma} = 2.21 \times 10^{-4}$ $MeV^{\frac{1}{2}}$

χ^2 = 2.16.

The errors on the fit parameters are as described in appendix C, method #1, and represent the excursion from the best-fit value of a parameter necessary to increase the total χ^2 by 1.0, while keeping all other parameters at their best-fit values. The 3-level R-matrix analysis fit

the data with a reduced χ^2 = 2 16. (Figure 24)

IV-F. Extrapolation to Stellar Energies:

The R-matrix theory gives the S-factor for all energies. To find the S-factor at 0.300 MeV, one must merely compute the R-matrix extrapolated value at 0.300 MeV. For the method and parameters outlined above and in appendix C, the best fit extrapolation yields $S_{E1}(300\ keV) = 40\ ^{+40}_{-34}$ keV-barns. This compares to previous results:

Redder et al. $S_{E1}(300\ keV) = 200\ ^{+280}_{-180}$ keV-barns
Dyer and Barnes $S_{E1}(300\ keV) = 140\ ^{+140}_{-120}$ keV-barns
Kettner et al. $S_{tot}(300\ keV) = 420\ ^{+160}_{-120}$ keV-barns

Both Redder et al. (RE87) and Dyer and Barnes (DY74) report E1 cross-sections and S-factors, and the comparison to the present E1 extrapolation is in excellent agreement. Kettner et al. (KE82) reports total cross-sections, so it is less obvious that a direct comparison is valid. Error analysis of the extrapolation was done differently for previous results, therefore the E1 data of Redder et al. (RE87) and Dyer and Barnes (DY74) was also fitted and extrapolated using the R-matrix method described for this measurement. The results are in appendix C. A weighted average of the $S_{E1}(300\ keV)$ values from the present measurement, And fits to Redder et al., and Dyer and Barnes from appendix C gives a result 100 ± 27 keV-barns. The average was computed using the bottom error bar for (RE87) and (DY74) while using the top

error bar for the present measurement.

Future measurements should emphasize determination of the α-width of the E_{cm} = 2.39 MeV, $J^{\pi} = 1^-$ resonance and determination of the size and sign of the interference between the high lying background states and the E_{cm} = 2.39 MeV resonance. Both of these can be determined by precision measurements of the E1 cross-section in the energy range 2.5 MeV < E_{cm} < 4.0 MeV. It is the high energy tail of the E_{cm} = 2.39 MeV resonance that is most poorly known. These high energy measurements will have the greatest impact in reducing the uncertainty in S_{E1}(300 keV).

References

(AJ85) F.Ajzenberg-Selove, Nuclear Physics **A433** (1985) No.1 1-158

(AJ86) F.Ajzenberg-Selove, Nuclear Physics **A460** (1986) No.1 1-148

(AN77) A.Anttila et al., Nuclear Instruments and Methods, **147** (1977) 501-505.

(AZ77) H.Anderson, J.Ziegler, Hydrogen: Stopping Powers in all Elements (1977) Pergammon Press

(BA80) C.Barnes, Laboratory Approaches to Nuclear Astrophysics, OAP-539

(BE69) P.Bevington, Data Reduction and Analysis for the Physical Sciences,(1969) McGraw-Hill

(BN77) K.Brown et al. SLAC 91, Rev.2 (1977) unpublished.

(BR77) A.Breskin, Nuclear Instruments and Methods **141**, (1977) 505-509

(CL68) G.J.Clark et al.,Nucl. Phys. **A110** (1968) 481

(CO65) S.Conte, C.deBoor, Elementary Numerical Analysis. (1965) McGraw-Hill

(CO81) T.Cormier,P.Stwertka, Nucl. Inst. and Meth. **184** (1981) 423-430

(EN81) H.Enge, Nucl. Inst. and Meth. **186** (1981) 413-422

(DY74) P.Dyer,C.Barnes, Nuclear Physics **A233**, 495-520

(FO83) W.Fowler, Nobel Lectures in Physics 1983,(Rev. Mod. Phys. **56** No.2, Part 1, April 1984.

(FU85) C.Funck, et al., Phys. Lett. **152**, 11 (1985)

(GO59) H.Gove, Nuclear Reactions, CH 6, Ed. P.Endt,M.Demeur. North-Holland Amsterdam.

(HA81) L.Harwood,J.Nolen, Nucl. Inst. and Meth. **186** (1981) 435-440

(HE79) W.Herrmannsfeldt,SLAC **226** (1979) unpublished.

References, Continued

(JO62) C.M.Jones et al., Nucl. Phys. **37** (1962) 1

(KE82) K.Kettner et al., Z. PHYS. A - Atoms and Nuclei **308**, 73-94 (1982)

(LA56) N.Lazar et al., Nucleonics **14** (1956) 52

(LA58) A.Lane, R.Thomas, Reviews of Modern Physics **30** No.2 (1958) 257-353

(LA83) K.Langanke,S.Koonin, Nuclear Physics **A410**, (1983) 334-348

(LA85) K.Langanke,S.Koonin, Nuclear Physics **A439**, (1985) 384-396

(MA71) J.Macdonald,F.Martin, Phys. Rev. A Vol **4** p1965 (1971)

(OS84) J.Osborne,A.Howard, Nuclear Instruments and Methods **222**, No.3 (1984) 428-430.

(PL87) R.Plaga et al., Nucl. Phys. **A465** (1987) No.2, 291-316

(RE85) A.Redder et al., Physical Review Letters **16**, Sept.,1985 1262-1265

(RE87) A.Redder et al., Nuclear Physics **A462**, (1987) 385-412

(SA77) M.Salomaa,H.Enge, Nucl. Inst. and Meth., **145** (1977) 279-282

(SA82) D.Sargood, Physics Reports **93** No.2, (1982) 61-116

(WE74) D.Weisser et al., Nuclear Physics **A235**, (1974) 460-469

(WO86) S.Woosley, Annual Review of Astronomy and Astrophysics Vol. **24** p.205 (1986)

(ZI80) J.Ziegler, Stopping Cross-Sections for Energetic Ions in All Elements,(1980) Pergamon Press.

APPENDIX A

Cascade Spectrum Fraction

The NaI(Tl) total efficiency is defined as the probability that a γ-ray, produced in the target area, is detected by the crystals in any part of the spectrum. The spectrum fraction is defined as the ratio of the number of events detected with energy above some cutoff energy (E_c) to the total number of events detected, regardless of the energy deposited in the detector. It is clear that the product of the total efficiency and the spectrum fraction gives the γ-ray counting efficiency.

To extend this definition to a two γ-ray cascade process is straightforward. The probability of detecting an event is clearly,

$$\varepsilon_{tot} = \varepsilon_{\gamma 1} + \varepsilon_{\gamma 2} - \varepsilon_{\gamma 1}\varepsilon_{\gamma 2} , \qquad \text{A-1}$$

where ε_t is the total efficiency for the cascade process, and ε_1 and ε_2 are the single γ-ray efficiencies for detecting the first and second γ-rays, respectively. The spectrum fraction is merely the ratio of the number of events detected above E_c to the total number of events detected. It is important to note that each cascade event produces two γ-rays, and the simultaneous detection of both γ-rays is considered a single event.

A single cascade event can have one of four outcomes. All or part of both γ-rays may be detected, all or part of γ_1 and none of γ_2 may be detected, all or part of γ_2 and none of γ_1 may be detected, and finally neither γ_1 nor γ_2 will be detected. This last is the trivial case and no more need be said. The cases in which exactly one γ-ray is detected contribute the single γ-ray spectrum fraction, appropriate for the energy of that γ-ray, to the cascade spectrum fraction. The contribution is weighted by the probability that the detection proceeds by that single γ-ray detection channel. For example, the portion of the spectrum fraction contributed by detecting γ_1 only is,

$$\frac{\varepsilon_{\gamma 1}(1-\varepsilon_{\gamma 2})}{\varepsilon_{\gamma 1} + \varepsilon_{\gamma 1} - \varepsilon_{\gamma 1}\varepsilon_{\gamma 2}} SF\left(\frac{E_c}{E_{\gamma 1}}\right) , \qquad \text{A-2}$$

where SF(x) is the single particle spectrum fraction as described in the text.

When both γ-rays are detected the contribution to the spectrum fraction is weighted by the the summing efficiency $\varepsilon_{\gamma 1}\varepsilon_{\gamma 2}$. The amount contributed at each point is a convolution of the two single particle spectrum fractions,

$$\frac{\varepsilon_{\gamma 1}\ \varepsilon_{\gamma 2}}{\varepsilon_{\gamma 1} + \varepsilon_{\gamma 2} - \varepsilon_{\gamma 1}\varepsilon_{\gamma 2}} \int_0^1 SF\left(1-x\frac{E_x}{E_{\gamma 2}} + z\frac{E_{\gamma 1}}{E_{\gamma 2}}\right) \frac{dSF(z)}{dz}\, dz . \qquad \text{A-3}$$

This integral is easily evaluated numerically using the form of the single γ-ray spectrum fraction as described in the text. The single γ-ray spectrum fractions for various energies were all taken to have the same functional form when the argument is scaled by the γ-ray energy.

Then the cascade spectrum fraction is,

$$SF_{ca}(x) = \frac{1}{\Delta}\Big(\varepsilon_{\gamma 1}(1 - \varepsilon_{\gamma 2})\ SF(x \frac{E_x}{E_{\gamma 1}}) + \varepsilon_{\gamma 2}(1 - \varepsilon_{\gamma 1})\ SF(x \frac{E_x}{E_{\gamma 2}})$$

$$+ \varepsilon_{\gamma 1}\varepsilon_{\gamma 2} \int_0^1 dz\ SF(1 - x \frac{E_x}{E_{\gamma 2}} + z \frac{E_{\gamma 1}}{E_{\gamma 2}}) \frac{dSF(z)}{dz} \Big) , \quad \text{A-4}$$

where E_x is the excitation energy of the excited state (It is also true that $E_x = E_{\gamma 1} + E_{\gamma 2}$ and $\Delta = \varepsilon_{\gamma 1} + \varepsilon_{\gamma 2} - \varepsilon_{\gamma 1}\varepsilon_{\gamma 2}$). Equation A-4 was evaluated for parameters appropriate for the $J^\pi = 4^+$ resonance at $E_x = 10.36$ MeV in $^{12}C(\alpha,\gamma)^{16}O$ and is plotted in Figure A-1 along with the measured spectrum fraction from the two-γ-ray cascade from that state. The agreement is satisfactory and gives confidence in the calculation.

APPENDIX B: γ_0 Yield Extraction

For any particular data point, TAC spectra were generated with cuts on E and ΔE of the recoil particle and on E_γ. Fifteen spectra were produced for which the only difference is the number of crystals allowed in coincidence as described in the text.

The number of single crystal γ_0-rays detected will stay constant regardless of the number of crystals added together, but the summing efficiency increases for larger numbers of crystals, so that the γ_C signal above the cutoff will increase. The detected yield for any combination of crystals is given by,

$$Y = \varepsilon_{\gamma 0}\, N_{\gamma 0}\, SF_{\gamma 0}\left(\frac{E_C}{E_X}\right) + (\varepsilon_{\gamma 1} + \varepsilon_{\gamma 2} - \varepsilon_{\gamma 1}\varepsilon_{\gamma 2})\, N_{\gamma C}\, SF_{Ca}\left(\frac{E_C}{E_X}\right) , \qquad \text{B-1}$$

where $\varepsilon_{\gamma 1}$ and $\varepsilon_{\gamma 2}$ are the total γ-ray detection efficiencies for the first and second cascade γ-rays respctively, N_{γ_0} and N_{γ_C} are the numbers of ground state and cascade events that occurred, and the SF(X) are the appropriate spectrum fractions.

The cutoff energy used in the analysis was E_C = 7.4 MeV. Then using equation A-4 and noting that terms 1 and 2 in equation A-4 vanish above about 6.9 MeV, equation B-1 becomes,

$$Y = \varepsilon_{\gamma O} N_{\gamma O} SF_{\gamma O}\left(\frac{E_C}{E_X}\right) + \varepsilon_{\gamma 1} \varepsilon_{\gamma 2} I N_{\gamma C} , \qquad B\text{-}2$$

where the I is the integral appearing in the third term of equation A-4.

For simplicity, $\varepsilon_{\gamma 1}$ and $\varepsilon_{\gamma 2}$ were taken as equal to ε_a, the efficiency for the ground state γ-ray. This is true to within a few percent for the energies and crystal geometry used in the present experiment. Also, the single crystal efficiencies for each of the four crystals were set equal to each other. It is useful at this point to define two quantities,

$$A = SF\left(\frac{E_C}{E_X}\right) \varepsilon N_{\gamma O} , \qquad B\text{-}3$$

$$B = \varepsilon^2 I N_{\gamma C} , \qquad B\text{-}4$$

where the parameters are the single-γ-ray, single-crystal values. In the single-crystal case, there are four crystals taken one at a time, so the total yield is four times what it would be for one crystal.

$$Y_1 = 4A + 4B . \qquad B\text{-}5$$

There are six ways to take four crystals two at a time, so the γ_O signal is 12 times the single-crystal value, but they are triple-counted by this method. The summing efficiency for each combination is four times the single-crystal summing. Therefore the yield is given by the following equation:

$$Y_2 = \frac{12A + 6*4B}{3} = 4A + 8B \ . \qquad \text{B-6}$$

For three-crystal summing, the summing efficiency is increased by a factor of nine, and there are four possible combinations. The direct-to-ground signal is again triple-counted and so increased by a factor of 12.

$$Y_3 = \frac{12A + 4*9B}{3} = 4A + 12B \ . \qquad \text{B-7}$$

There is only one combination of four crystals so the yield is,

$$Y_4 = 4A + 16B \ . \qquad \text{B-8}$$

Note that the first term in equations B-5 through B-8 is constant, but the second term increases linearly with the number of crystals. This method effectively divides equation B-1 by a number proportional to the single γ-ray detection efficiency, giving a function that is linear in the efficiency with a y-intercept equal to the γ_0 yield. Some examples of the yield data and the extrapolation to zero crystal size are shown in Figure B-1.

The error analysis for this method is not trivial since the data are not independent. The method used was iterative. The four different yields, as extracted, were plotted and extrapolated to zero efficiency. This approximate intercept was subtracted from the four data points, and the resulting incremental yields were fitted with a linear least-squares

fit, with only the square-root of the incremental yield as the error. The new intercept was close to zero and was added to the approximate intercept to give the extrapolated yield. The error was taken as,

$$\sigma_Y^2 = \sigma_{intercept}^2 + N_{incremental} , \qquad B-9$$

where $\sigma_{intercept}$ is the uncertainty in the intercept due to the least squares extrapolation and $N_{incremental}$ is the projected intercept for counting statistics.

Appendix C. S-Factor Extrapolated Error:

I. Parameters:

The four parameters required for the fit were selected as described in the text using the 3-level R-matrix formalism. The errors assigned to these parameters must in some way represent the sensitivity of the χ^2 to a change in each of the parameters. Two methods of assigning errors suggest themselves, neither of which is correct in every case. Method 1 is to hold all but one parameter constant at the best-fit value and vary the one parameter until the total χ^2 of the S-factor curve produced increases by 1.0. Method 2 is to find the value of a parameter necessary to increase the total χ^2 by 1.0 while allowing the other parameters to minimize χ^2. Neither method is entirely correct since the range of parameters generated by method 1 will tend to underestimate the "volume of variability" in parameter space, while method 2 will tend to overestimate this volume.

As a more concrete example, consider the case of a two parameter fit to some data. We can then place the origin of our coordinate system at the values of the parameters that minimize the total χ^2 by measuring our parameters as differences from their best-fit values. There then exists a closed curve of parameter values, such that $\chi^2_{tot} = \chi^2_{min} + 1$. This curve may look like the curve in Figure C-1a or C-1b. In the case of Figure C-1a, the parameters are completely independent, and both methods agree. In Figure C-1b the two methods disagree, and the amount

of disagreement gives some idea of the correlation between the parameters. The errors on the parameters determined in these two ways are:

Parameter; $MeV^{\frac{1}{2}}$	Method 1 $MeV^{\frac{1}{2}}$	Method 2 $MeV^{\frac{1}{2}}$
$\gamma_{1_\alpha} = 0.19$	$^{+0.03}_{-0.03}$	$^{+0.18}_{-0.56}$
$\gamma_{2_\alpha} = 0.65$	$^{+0.02}_{-0.02}$	$^{+0.04}_{-0.05}$
$\gamma_{2_\gamma} = -.000133$	$^{+.000003}_{-.000003}$	$^{+.000006}_{-.000006}$
$\gamma_{3_\gamma} = -.0011$	$^{+.00010}_{-.00011}$	$^{+.00057}_{-.00071}$

In the case of the 3-level, R-matrix analysis, the values of the fit parameters have no special physical significance, since the parameters can be radically altered by selecting different values of B and R without affecting the χ^2 or the physics. Hence, the errors on these parameters are merely a convenience to help determine the uncertainty in the physically relevant S_{E1}(300 keV) value.

II. Extrapolation:

The predicted value of S_{E1}(300 keV) is determined by merely evaluating the 3-level, R-matrix formula at E_{cm} = 0.3 MeV. The value so obtained is 40 keV-barns. The uncertainties in such an extrapolation is more difficult to determine.

The errors on S_{E1}(300 keV) are determined with a Monte Carlo technique. A distribution of parameter values were generated for each parameter in the fit. Then for each iteration, a value was selected at random from each of the distributions, and the value of S_{E1}(300 keV) and the χ^2_{tot} was determined.

There are correlations between the parameters that can prevent any arbitrary selection of parameters from resulting in a small χ^2. The resultant χ^2 is an indication of the validity of the S_{E1}(300 keV) value obtained. Thus the correlations between parameters are taken into account by monitoring the χ^2 of the fit to the S_{E1} data. In light of this, the folowing histograms were generated:

1) A histogram of the number of occurrences of each S(300 keV) value. (The bin size used was 1 keV-barn.)
2) A histogram of the frequency of occurrence of each value of S(300 keV), where the number to increment the appropriate bin by was $\chi^2_{min}/\chi^2_{tot}$. This is the "$\chi^2$ weighted" histogram.
3) A histogram of the frequency of occurrence of each S(300 keV) value in which the resulting χ^2_{tot} was within 1.0 of χ^2_{min}.

The three histograms generated give an estimate of the range of variability of S(300 keV) allowed by the data. Samples of some of the histograms are shown in Figure C-2.

The distribution of the parameter values was chosen to be gaussian with the FWHM = the error bar as determined by method #2. For asymmetric error bars, this requires different FWHM values above and below the

best-fit value. The two half-gaussians were normalized to equal areas. The selection of the parameters was random, weighted by this distribution. One hundred thousand sets of parameters were selected, and the results of the three histograms are:

Histogram #1 $S_{E1}(300\ keV) = 40\ ^{+45}_{-37}$ kev-barns,

Histogram #2 $S_{E1}(300\ keV) = 40\ ^{+40}_{-34}$ keV-barns,

Histogram #3 $S_{E1}(300\ keV) = 40\ ^{+17}_{-10}$ keV-barns.

All of the methods give comparable results. Histogram #2 was chosen to represent the errors allowed by the data since the only constraint is the intuitively reasonable $1/\chi^2$ weighting.

III. Other Data:

Both Redder et al. (RE87) and Dyer and Barnes (DY74) report E1 cross section data. The analysis above has been applied to their data. As noted in the text, they both used 3-level, R-matrix analysis with only 3 free parameters. The analysis described above has been carried out for both data sets for three and four parameter fits. The motivation for this is that this error treatment is expected to give tighter error bars on $S_{E1}(300\ keV)$ than the treatment reported by Dyer and Barnes or by Redder et al., and a direct comparison between data sets is desired. The tighter errors result from the fact that previous measurements determined errors by letting the χ^2_{tot} of the fit vary by the number of degrees of freedom while the present analysis allows χ^2_{tot} to vary by 1.0 only.

Redder's E1 data resulted in:

3-parameter, $S_{E1}(300\ keV) = 172 \pm 50$ keV-b, $\chi^2_\nu = 2.96$,

4-parameter, $S_{E1}(300\ keV) = 205 \pm 61$ keV-b, $\chi^2_\nu = 2.99$,

Where ν equals the number of degrees of freedom. Dyer and Barnes E1 data generated:

3-parameter, $S_{E1}(300\ keV) = 138\ ^{+27}_{-58}$ keV-b, $\chi^2_\nu = 1.83$,

4-parameter, $S_{E1}(300\ keV) = 147\ ^{+49}_{-54}$ keV-b, $\chi^2_\nu = 1.92$.

The reason for the poor χ^2 to Redder et al.'s data is not clear; the simplest explanation is that the error bars reported were underestimated or that the model is wrong. Under the assumption of underestimated error bars, a 10% random error was added to the stated errors, and the four parameter fit was redone. This will tend to underemphasize the high statistics data.

4-parameter, $S_{E1}(300\ keV) = 245\ ^{+72}_{-70}$ keV-b, $\chi^2_\nu = 1.00$.

An alternate approach to treating poor χ^2 fits is to simply multiply the error bar by $\sqrt{\chi^2_\nu}$. By this method the Redder data results in:

3-parameter, $S_{E1}(300\ keV) = 172 \pm 86$keV-b ,

4-parameter, $S_{E1}(300\ \text{keV}) = 205 \pm 103$ keV-b .

Note that only Kettner et al.'s (KE82) value of $S_{E1+E2}(300\ \text{keV})$ $= 420\ ^{+160}_{-120}$ keV-barns is more than 2σ away from the present measurement.

Appendix D

Derivation of the Cross-Section Formula:

The yield of the $^{12}C(\alpha,\gamma)^{16}O$ reaction as measured in this experiment has contributions from both the E1 and E2 components. The goal is to extract a formula for the E1 component in terms of measured or known quantities.

It is clear that for a single multipole, the cross-section is given by:

$$\sigma_\ell = \frac{Y_\ell}{\varepsilon_p \, \varepsilon_{\gamma t}(E\ell)} \, , \qquad \text{D-1}$$

where σ_ℓ is the cross-section for the ℓ'th multipole, ε_p is the product of all the efficiencies and other factors that do not depend upon ℓ, ($\varepsilon_p = N_b \; t \; \varepsilon_{cuts} \; \varepsilon_{tim} \; \varepsilon_{spf} \; Q_f$) and $\varepsilon_{\gamma t}(E\ell)$ is the γ-ray/recoil particle transport efficiency for the ℓ'th multipole.

We measure the yield $Y = Y_1 + Y_2$. Another relation between Y_1 and Y_2 is given by taking the ratio of equation D-1 with itself:

$$\frac{\sigma_2}{\sigma_1} = \frac{Y_2 \; \varepsilon_{\gamma t}(1)}{Y_1 \; \varepsilon_{\gamma t}(2)} \, , \qquad \text{D-2}$$

or

$$Y_2 = Y_1 \, \frac{\sigma_2 \; \varepsilon_{\gamma t}(2)}{\sigma_1 \; \varepsilon_{\gamma t}(1)} \, . \qquad \text{D-3}$$

Combining D-3 with $Y = Y_1 + Y_2$ gives,

$$Y_1 = Y \left(1 + \frac{\sigma_2 \, \varepsilon_{\gamma t}(2)}{\sigma_1 \, \varepsilon_{\gamma t}(1)} \right)^{-1} . \qquad \text{D-4}$$

Then the E1 cross-section is,

$$\sigma_1 = \frac{Y}{\varepsilon_p \, \varepsilon_{\gamma t}(1) \left(1 + \frac{\sigma_2 \, \varepsilon_{\gamma t}(2)}{\sigma_1 \, \varepsilon_{\gamma t}(1)} \right)} , \qquad \text{D-5}$$

so that

$$\sigma_1 = \frac{Y \left(1 + \frac{\sigma_2 \, \varepsilon_{\gamma t}(1)}{\sigma_1 \, \varepsilon_{\gamma t}(2)} \right)^{-1}}{N_b \, t \, \varepsilon_{cuts} \, \varepsilon_{tim} \, \varepsilon_{spf} \, Q_f \, \varepsilon_{\gamma t}(1)} , \qquad \text{D-6}$$

just as used in section IV. (Note that the target thickness is in particles/cm^2, and all other terms are dimensionless so that σ_1 is an area.)

Tables

Table 1, E1 Cross-Section

E_{cm} MeV	σ (nbarns)	$\delta\sigma$ (nbarns)
3.287	0.55	0.41
2.901	3.3	0.9
2.786	2.9	0.5
2.589	20.2	3.1
2.490	32.1	3.4
2.389	42.6	3.6
2.288	35.7	4.7
2.190	24.7	3.4
2.091	10.4	1.7
1.891	2.5	0.5
1.689	1.02	0.2
1.490	0.28	0.07
1.291	0.16	0.03

Table 2, E1 S-Factor

E_{cm}	S (keV-barns)	δS (keV-barns)
3.287	0.15	0.11
2.901	1.68	0.48
2.786	1.85	0.33
2.589	18.6	2.8
2.490	36.6	3.9
2.389	61.2	5.2
2.288	65.8	8.7
2.190	59.0	8.1
2.091	32.8	5.4
1.891	15.1	3.0
1.689	12.9	2.5
1.490	8.63	2.24
1.291	15.4	2.9

Figure 1

Partial Level Diagram

Partial level diagram relevant to the $^{12}C(\alpha,\gamma)^{16}O$ reaction. The energy range near the three upper states in ^{16}O of $J^{\pi} = 4^{+}$, 2^{+}, and I is investigated. Note the two, barely subthreshold states at 7.119 and 6.917 MeV. These are the two states that are expected to dominate the α-capture cross-section at stellar energies.

Figure 1

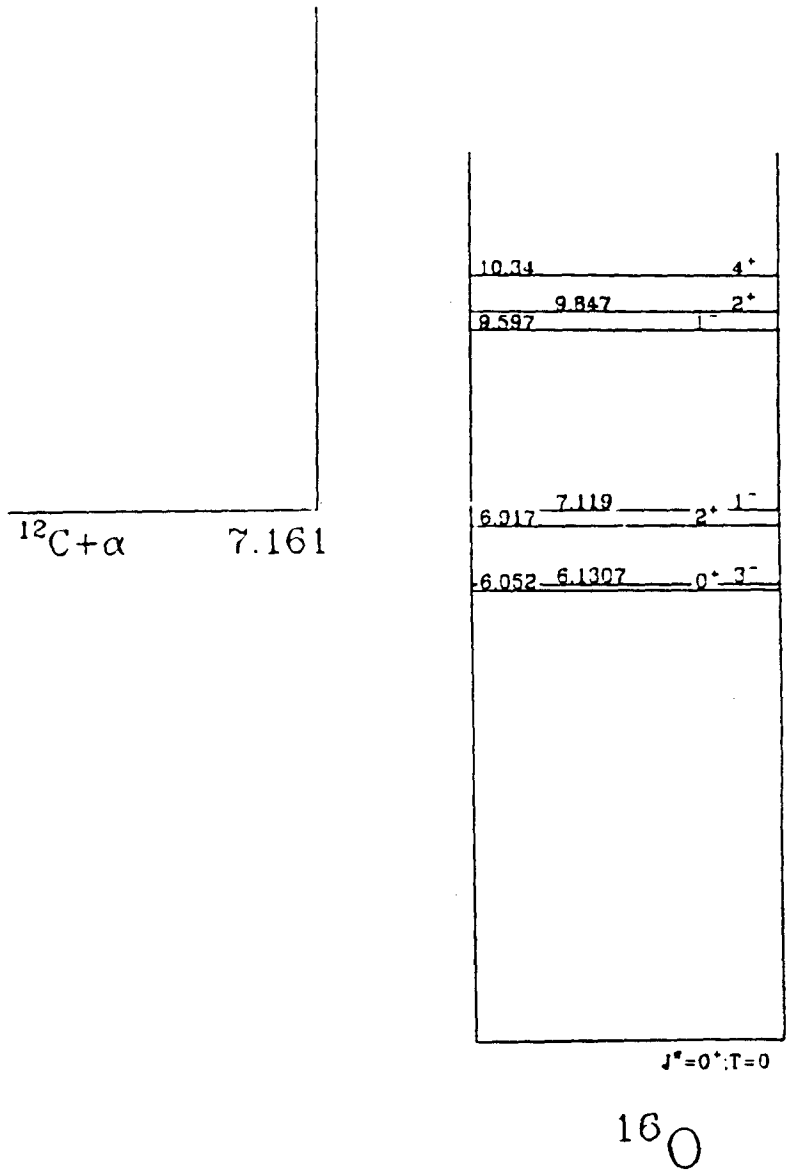
10.34
4+
9.847
2+
9.597
1-
7.119
1-
6.917
2+
6.052
6.1307
0+
3-
J^π=0^+;T=0
12C+α
7.161
16O

Figure 2

Schematic of Target System

Schematic of the Gas Handling System. Typical Helium pressures are:

Region 1	2.5 torr
Region 2	0.20 torr
Region 3	2×10^{-5} torr
Region 4	0.02 torr
Region 5	2×10^{-4} torr

Further details in the text.

Figure 2

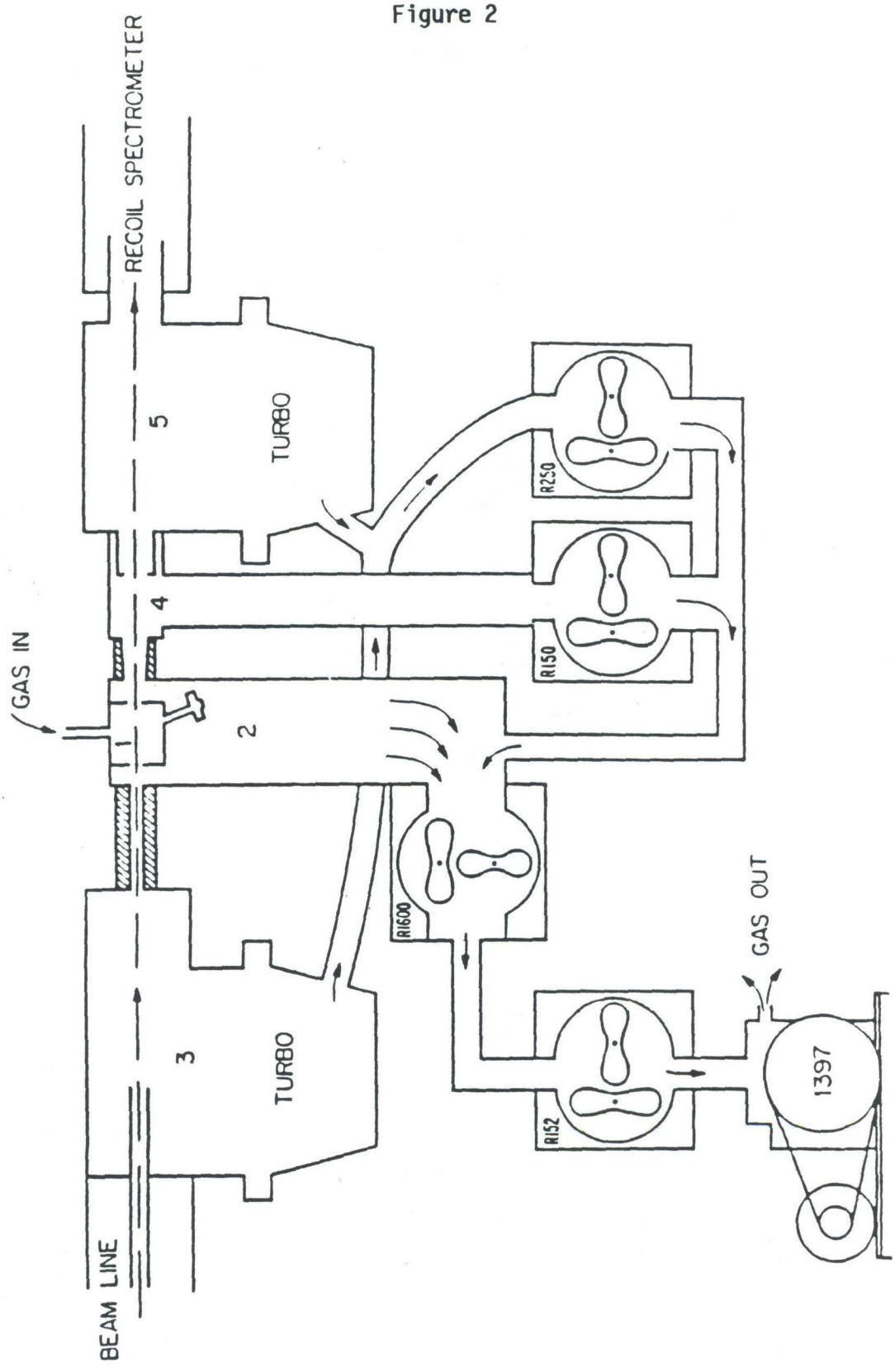
RECOIL SPECTROMETER
GAS IN
BEAM LINE
TURBO
TURBO
1
2
3
4
5
R1600
R150
R250
R152
1397
GAS OUT

Figure 3

Close-up of Target Cell

Cross section of the target can and target cell. Note the low profile and compact design. The outer can and target top are made of stainless steel. The inner target cell is made of copper.

The tubes on the outside of the target cell are for carrying liquid nitrogen for cooling the gas. This method of slowing the leakage of the gas has not yet been successfully demonstrated.

Figure 3

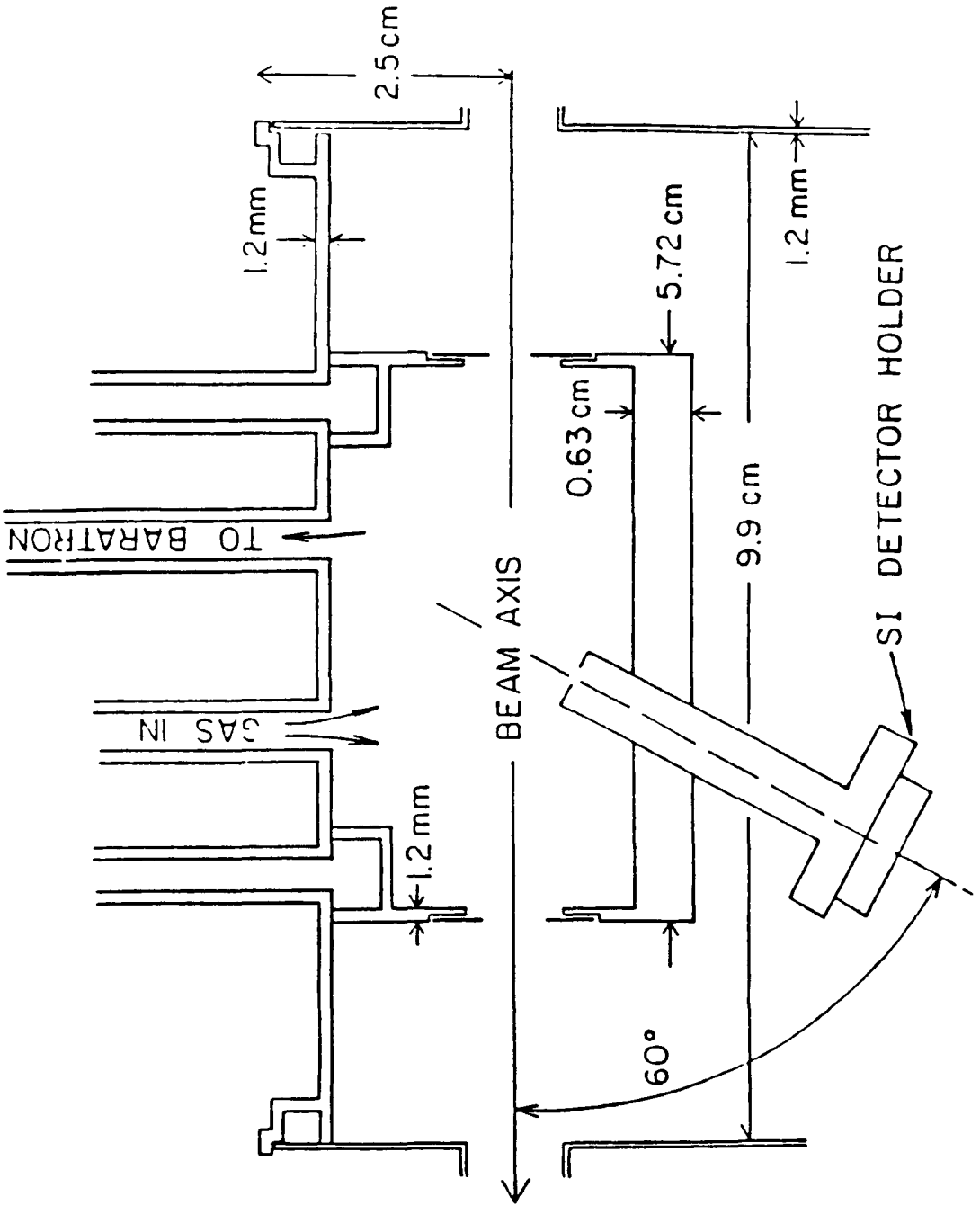
2.5 cm
1.2 mm
TO BARATRON
GAS IN
1.2 mm
BEAM AXIS
0.63 cm
5.72 cm
9.9 cm
1.2 mm
SI DETECTOR HOLDER
60°

Figure 4

Target and Detector Geometry

Section transverse to the beam direction, showing the geometry through the target cell, detector assembly, and lead "castle". The roller bearings allow each side of the cluster to be withdrawn for easy access to the target chamber.

The cyrstal placement is not completely right-left symmetric. The bottom left crystal is moved 4.1 cm up-beam to make room for some of the vacuum apparatus.

Figure 4

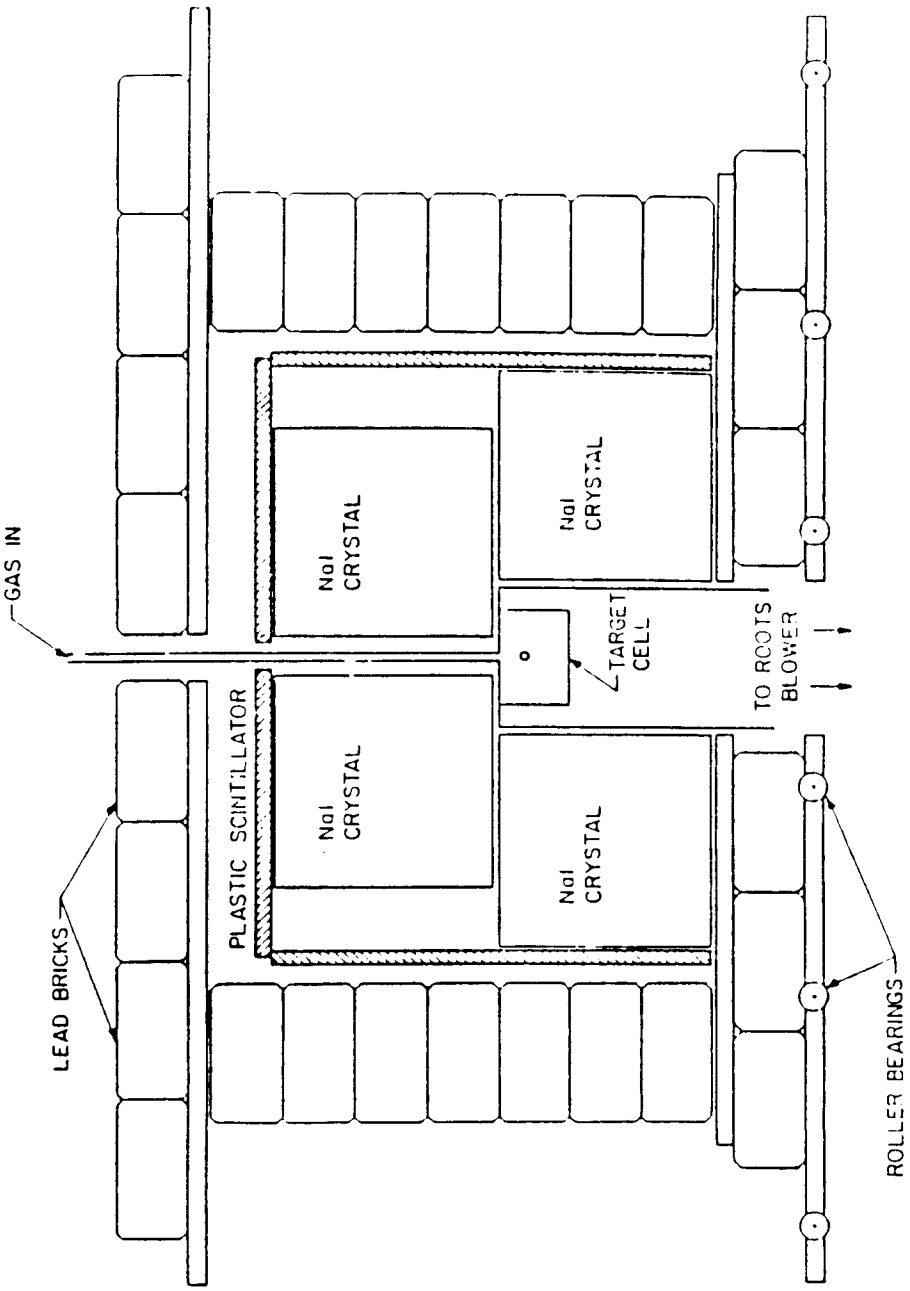
GAS IN
NaI CRYSTAL
NaI CRYSTAL
TARGET CELL
TO ROOTS BLOWER
PLASTIC SCINTILLATOR
NaI CRYSTAL
NaI CRYSTAL
LEAD BRICKS
ROLLER BEARINGS

Figure 5

Diagram of Photo Tube Bases

Basing Diagram for the NaI(Tl) Photomultipliers. The energy signal is picked off the sixth dynode. The emmitter-follower circuit is necessary to drive the 50 Ω timing-filter-amplifier input without loading the dynode chain.

Figure 5

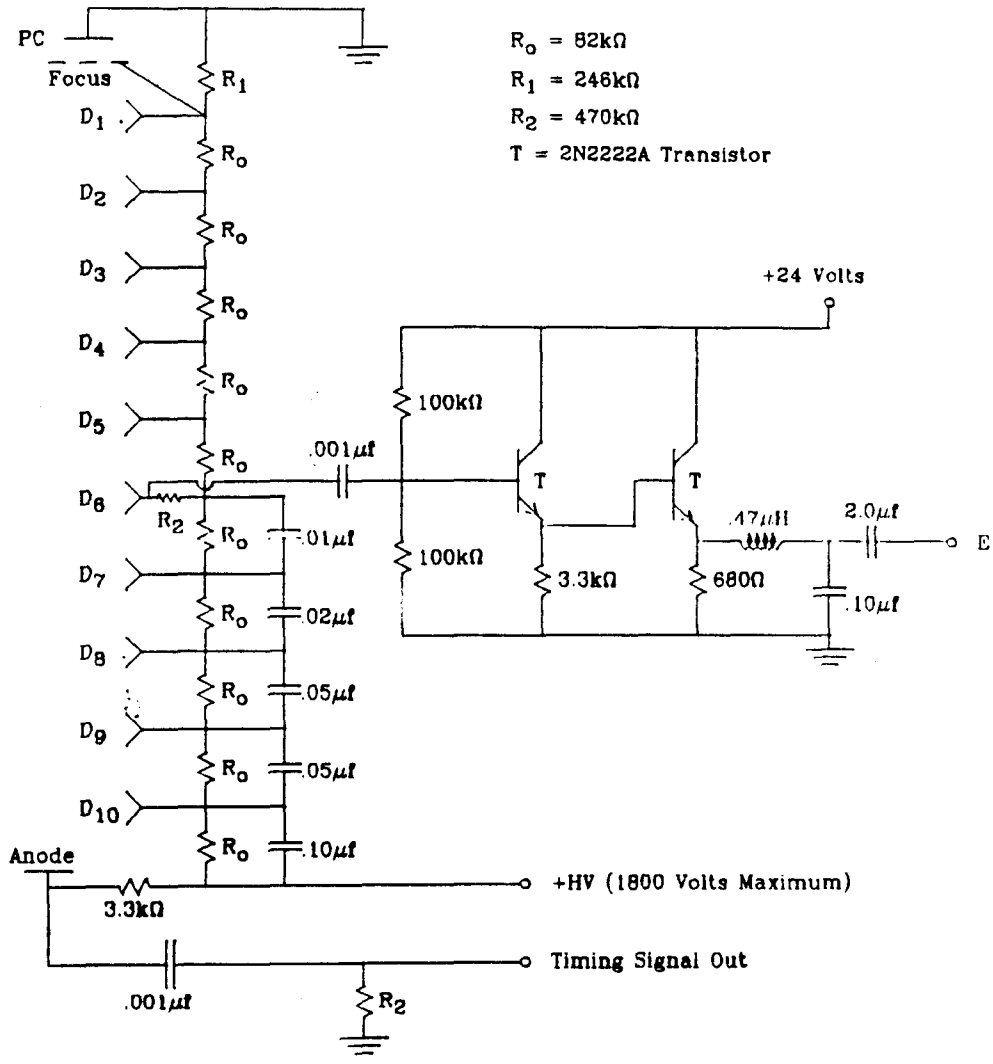
PC
Focus
D1
D2
D3
D4
D5
D6
D7
D8
D9
D10
Anode
R1
Ro
R2
3.3kΩ
.001μf
.01μf
.02μf
.05μf
.05μf
.10μf
100kΩ
100kΩ
T
T
3.3kΩ
680Ω
.47μH
2.0μf
.10μf
+24 Volts
E
+HV (1800 Volts Maximum)
Timing Signal Out
.001μf
R2
Ro = 82kΩ
R1 = 246kΩ
R2 = 470kΩ
T = 2N2222A Transistor

Figure 6

Recoil Separator

Top view of the Recoil Separator showing the layout and the scale of the apparatus.

Figure 6

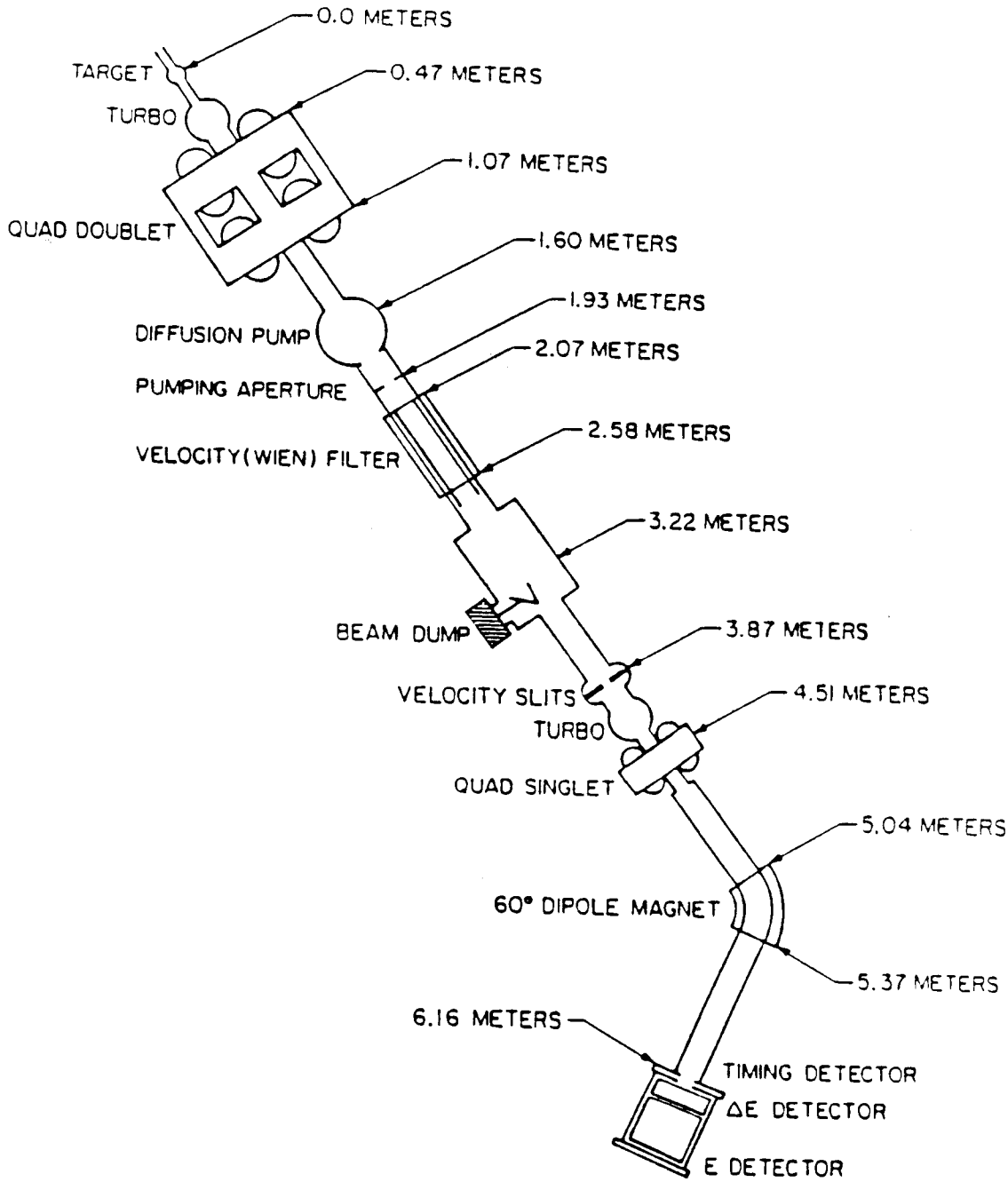
0.0 METERS
TARGET
0.47 METERS
TURBO
1.07 METERS
QUAD DOUBLET
1.60 METERS
1.93 METERS
DIFFUSION PUMP
2.07 METERS
PUMPING APERTURE
2.58 METERS
VELOCITY(WIEN) FILTER
3.22 METERS
BEAM DUMP
3.87 METERS
VELOCITY SLITS
4.51 METERS
TURBO
QUAD SINGLET
5.04 METERS
60° DIPOLE MAGNET
5.37 METERS
6.16 METERS
TIMING DETECTOR
ΔE DETECTOR
E DETECTOR

Figure 7

Calculated Beam Optics

Diagram of the first order Recoil Separator beam optics as calculated using the code TRANSPORT. The upper half of the diagram is the radial displacement from the axis in the x or horizontal direction, the lower half is the y or vertical direction.

This type of calculation was done for a representative range of energies and initial conditions. The Recoil Separator was designed around these calculations. (The vertical axis is in mm)

Figure 7

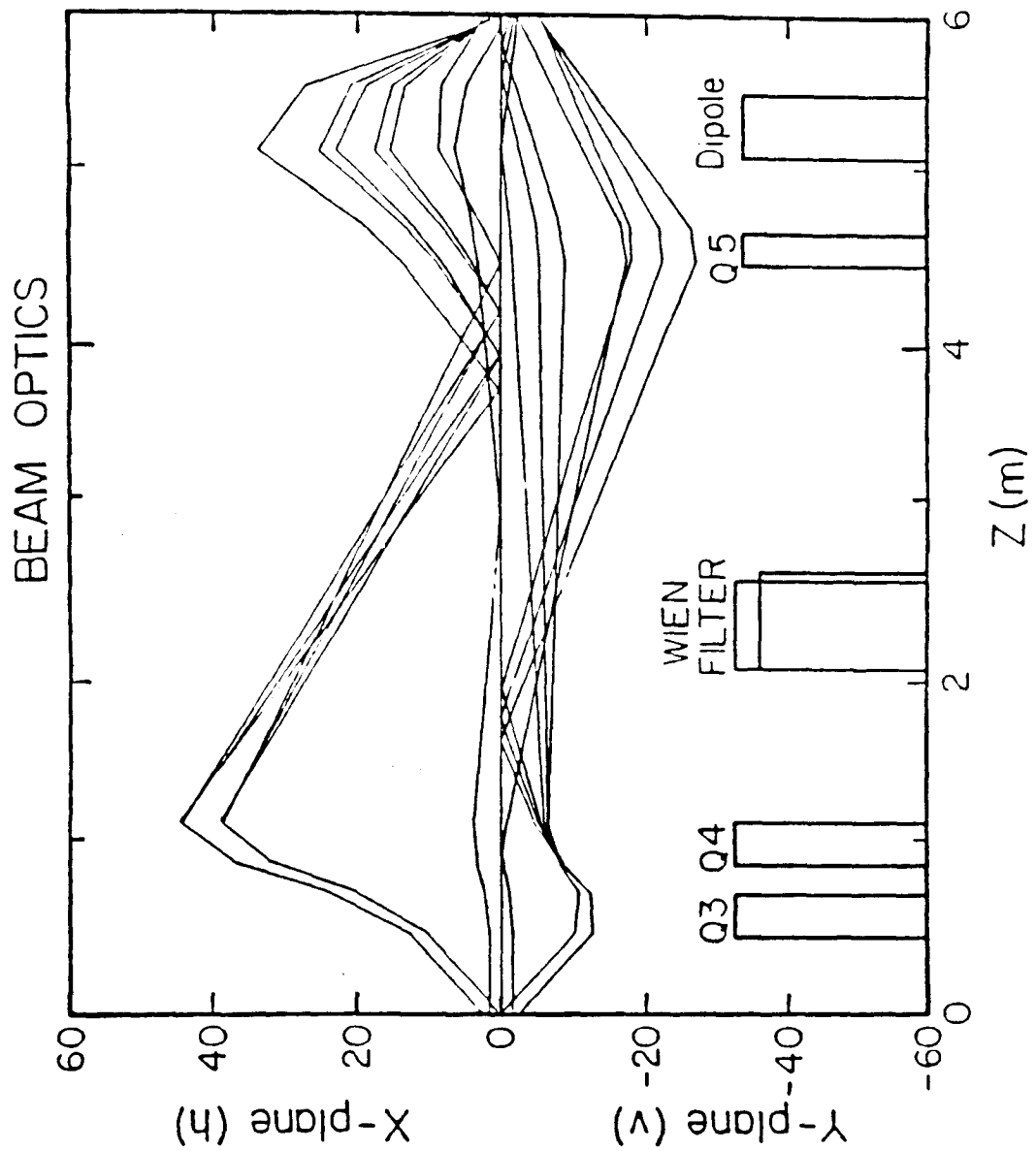
BEAM OPTICS
X-plane (h)
Y-plane (v)
Z (m)
Q3
Q4
WIEN FILTER
Q5
Dipole
60
40
20
0
-20
-40
-60
0
2
4
6

Figure 8

Section of Electrostatic Plates

Cross section of Wien filter electrostatic plates. The plates extend 60 cm in the beam direction. The shape of the plates was chosen to optimize the region of uniform field between the plates. The calculations were performed using the code GUN (HE79). The stated dimensions were held within 0.005 cm. Over the whole length, the surface was parallel to within 0.005 cm.

Figure 8

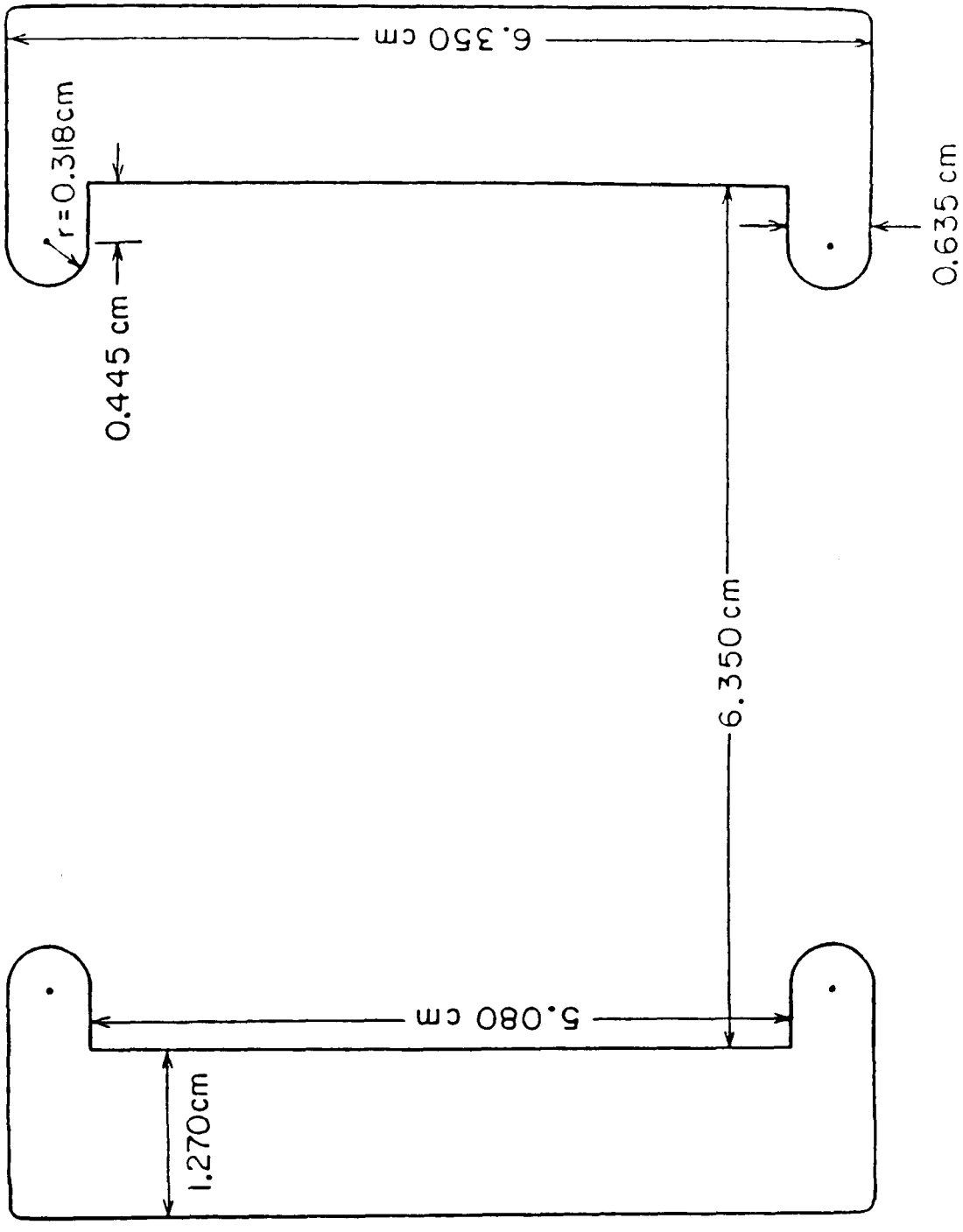

Figure 9

Recoil Detector

Diagram of the gas ionization chamber that houses the timing detector and the E and ΔE detectors. The pressure of isobutane used is in the range 5.0 to 8.5 torr. The pressure selected depends upon the energy of the recoil ions. The pressure is such that the recoil ion stops midway along the energy (E) detector plate.

Figure 9

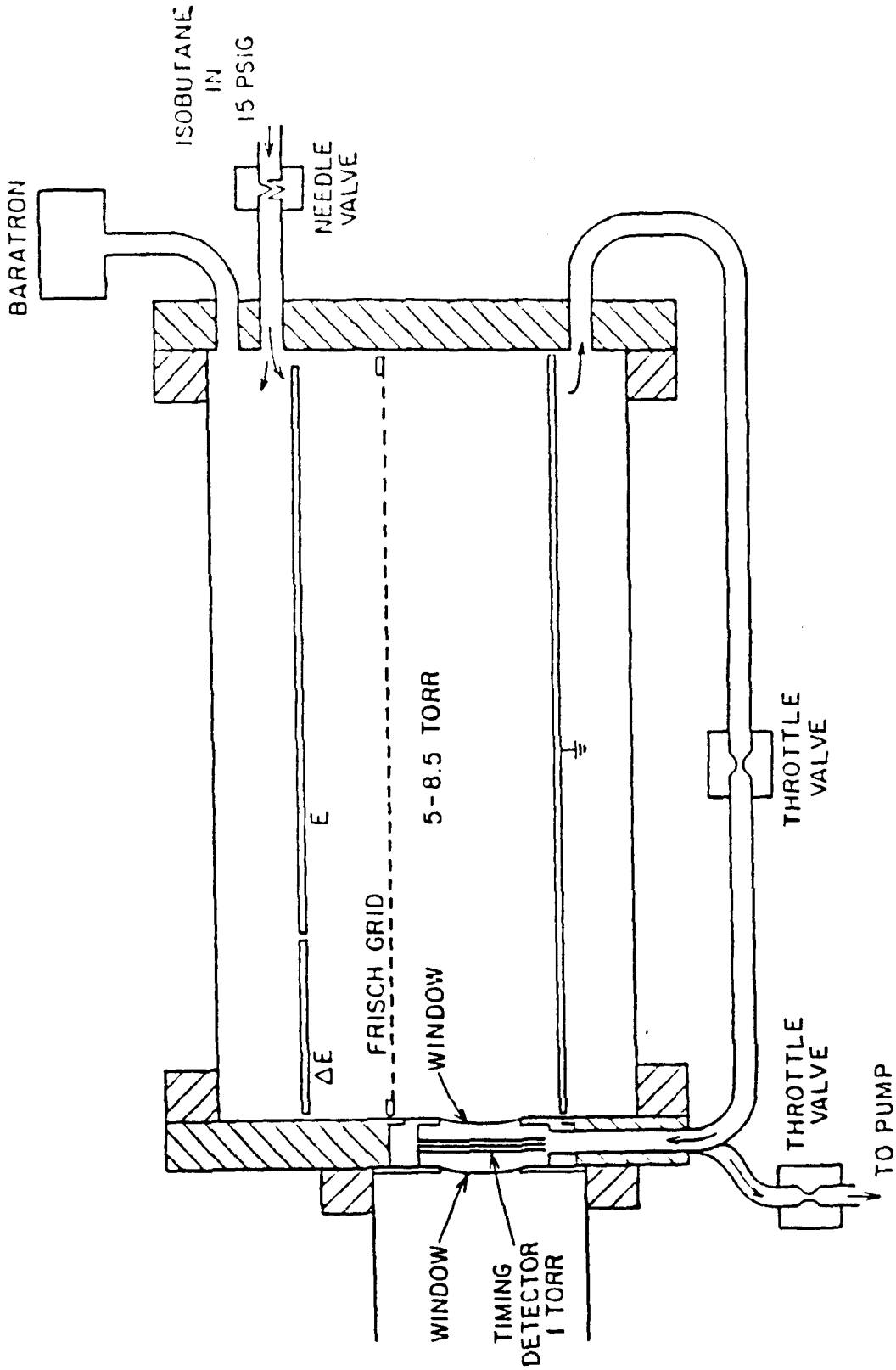
ISOBUTANE
IN
15 PSIG
NEEDLE
VALVE
BARATRON
E
ΔE
FRISCH GRID
5-8.5 TORR
WINDOW
THROTTLE
VALVE
THROTTLE
VALVE
TO PUMP
WINDOW
TIMING
DETECTOR
1 TORR

Figure 10

Beam Power Calorimeter

Schematic of the beam power calorimeter and its bridge circuit. The D.C. power is supplied by a NIM bin power supply. The variable resistor supplies current to zero the output of the two AD590 temperature transducers when they are at the same temperature. This assures an accurate measurement of ΔT.

Figure 10

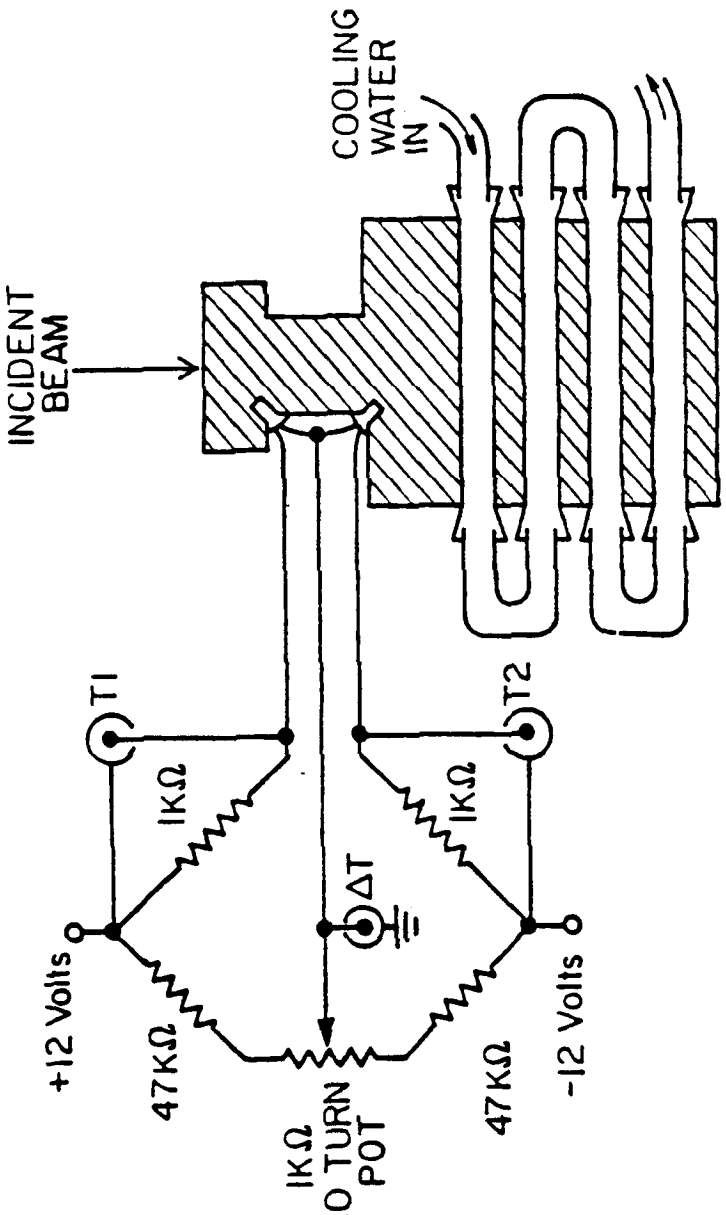
COOLING WATER IN
INCIDENT BEAM
T1
T2
1KΩ
1KΩ
ΔT
+12 Volts
-12 Volts
47KΩ
47KΩ
1KΩ 10 TURN POT

Figure 11

Electronics

Diagram of the electronics used for this measurement, showing the four detector systems used. A summary of notation followes.

DISC - level discriminator

S(N) - N'th scaler, counts logic pulses

SCA OUT - single channel analyzer output

Coinc. - Majority logic unit

spec amp - ORTEC model 571 spectroscopy amplifier

AD811 - ORTEC model AD811 multichannel ADC

3511 - LeCroy model 3511 ADC

Figure 11

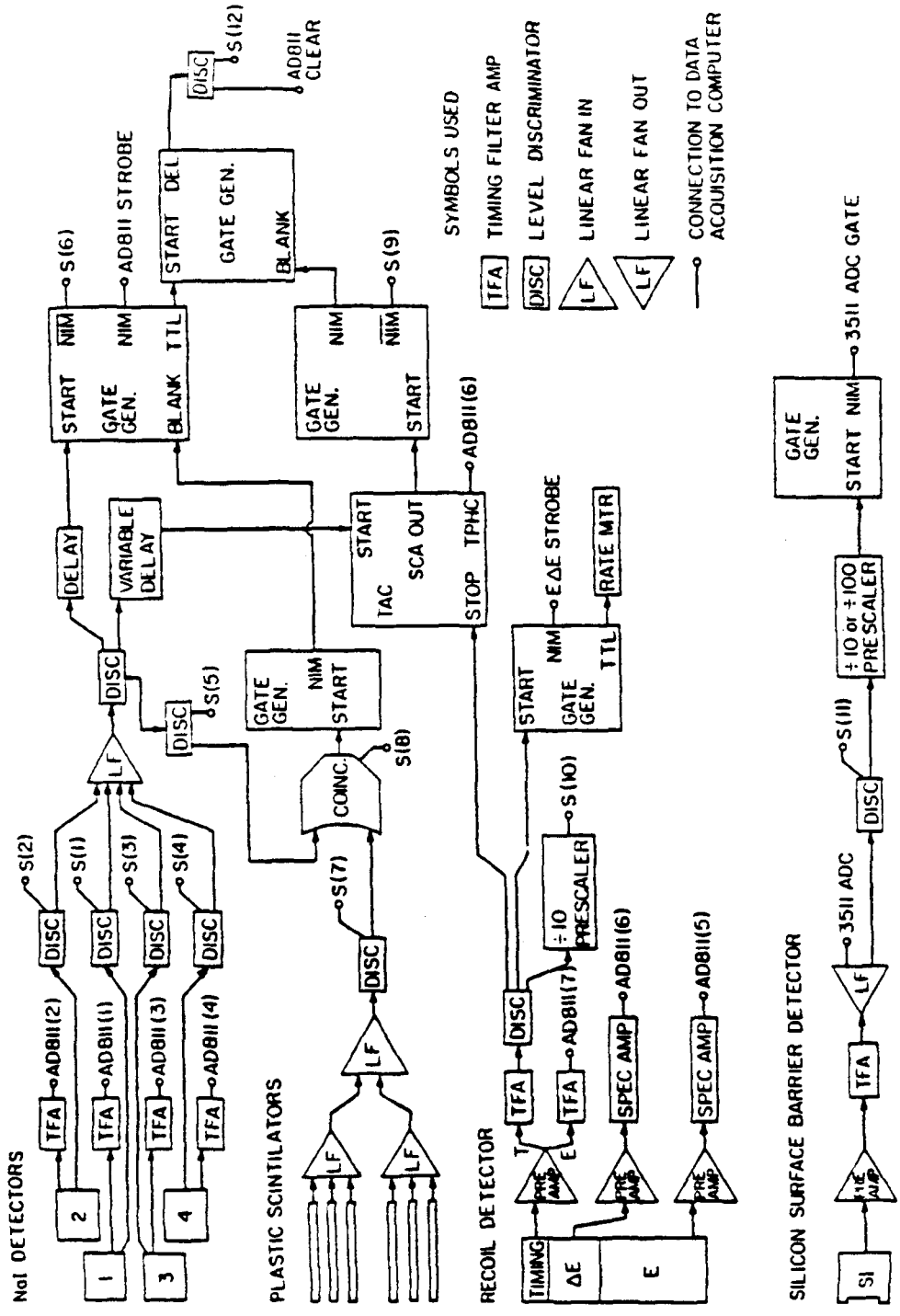
NaI DETECTORS
PLASTIC SCINTILATORS
RECOIL DETECTOR
SILICON SURFACE BARRIER DETECTOR
SYMBOLS USED
TIMING FILTER AMP
LEVEL DISCRIMINATOR
LINEAR FAN IN
LINEAR FAN OUT
CONNECTION TO DATA ACQUISITION COMPUTER
AD811 STROBE
AD811 CLEAR
S(1)
S(2)
S(3)
S(4)
S(5)
S(6)
S(7)
S(8)
S(9)
S(10)
S(11)
S(12)
AD811(1)
AD811(2)
AD811(3)
AD811(4)
AD811(5)
AD811(6)
AD811(7)
E ΔE STROBE
3511 ADC
3511 ADC GATE
DELAY
VARIABLE DELAY
START
STOP
TAC
SCA OUT
TPHC
GATE GEN.
START DEL
BLANK
RATE MTR
PRESCALER
SPEC AMP
PRE AMP
TIMING
ΔE
E
SI

Figure 12

γ-Ray Detection Efficiency

NaI(Tl) crystal total efficiency as a function of γ-ray energy for isotropic (i), quadrupole (q), and dipole (d) γ-ray distributions. The effects for the extended source distribution are included which has the result of lowering the total efficiency by ~3-5%, compared to that for a point source located at the center of the target cell.

The curve drawn is the calculated efficiency for the angular distribution as marked. The three points indicated are the measured efficiencies for isotropic γ-rays as described in the text.

Figure 12

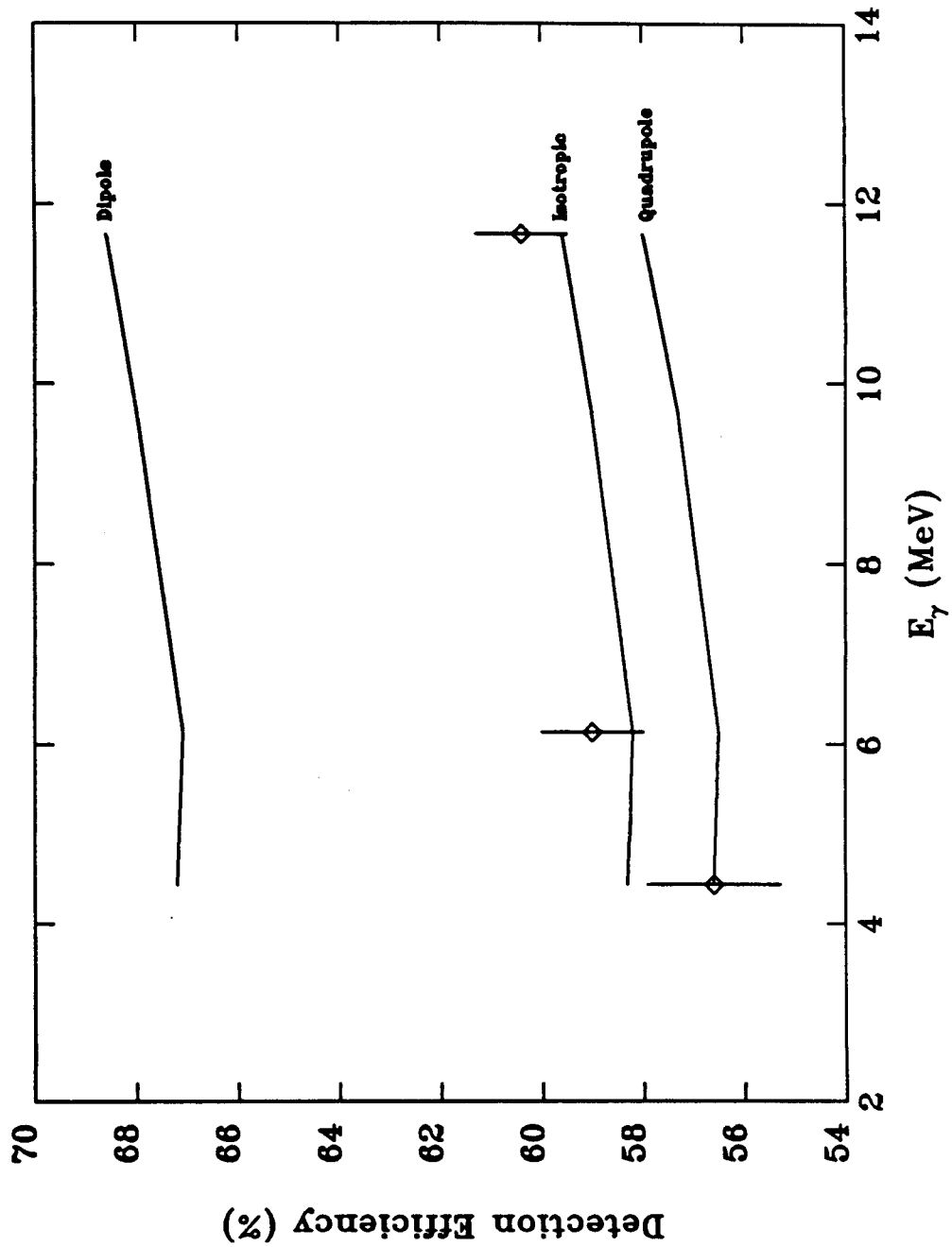
Dipole
Isotropic
Quadrupole
Detection Efficiency (%)
E_γ (MeV)
70
68
66
64
62
60
58
56
54
2
4
6
8
10
12
14

Figure 13

Spectrum Fraction Curve

NaI(Tl) spectrum fraction as a function of energy fraction. The data shown are for 4.4 MeV, 6.13 MeV, and 11.7 MeV γ-rays. This is the spectrum fraction for zero summing as described in the text. The curve drawn is a polynomial fit to the data which is used in the cascade spectrum fraction calculation of appendix A.

Figure 13

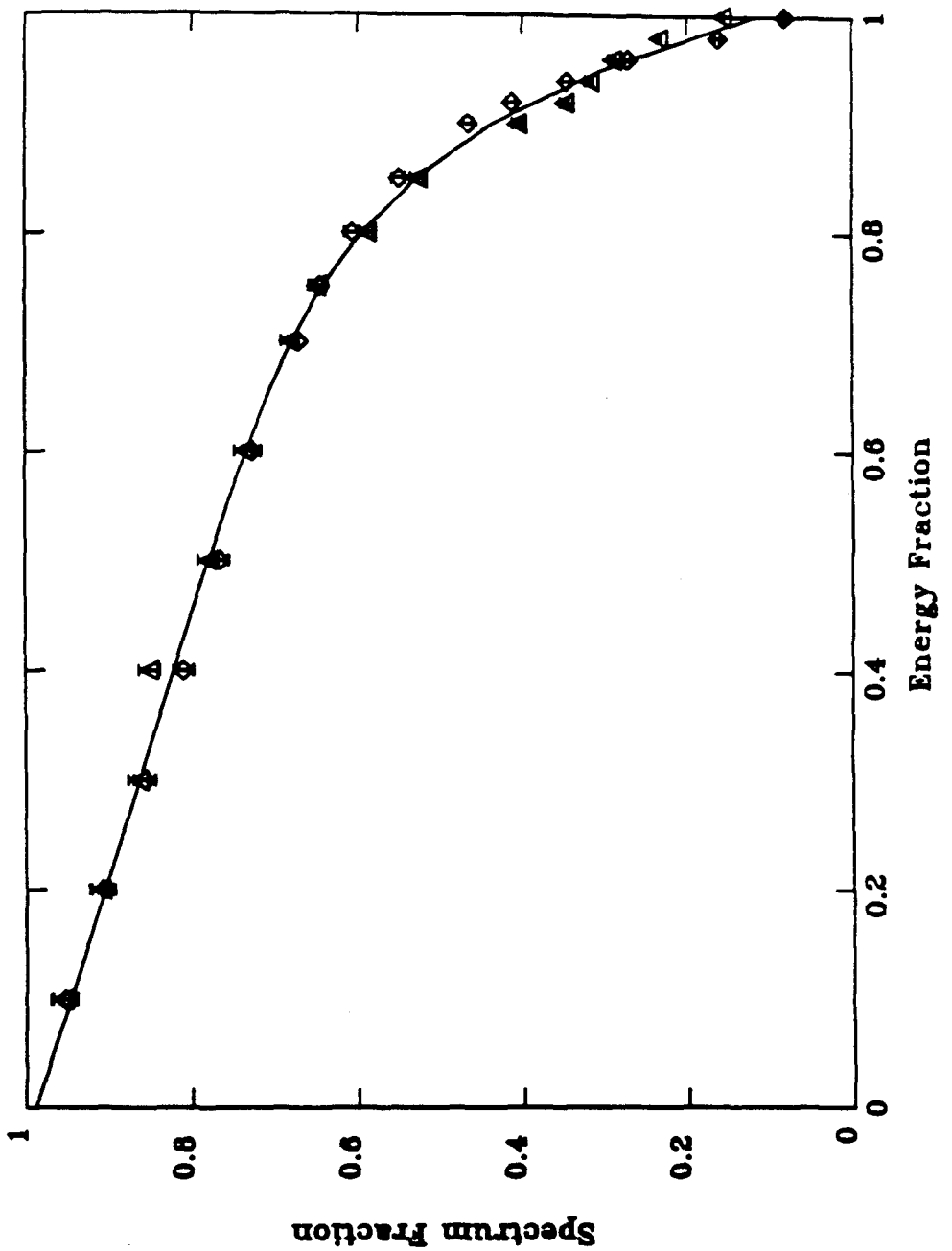

Figure 14

Spectrum Fractions Used

These are the values extracted from the Spectrum Fraction Curve for use in this analysis.

Figure 14

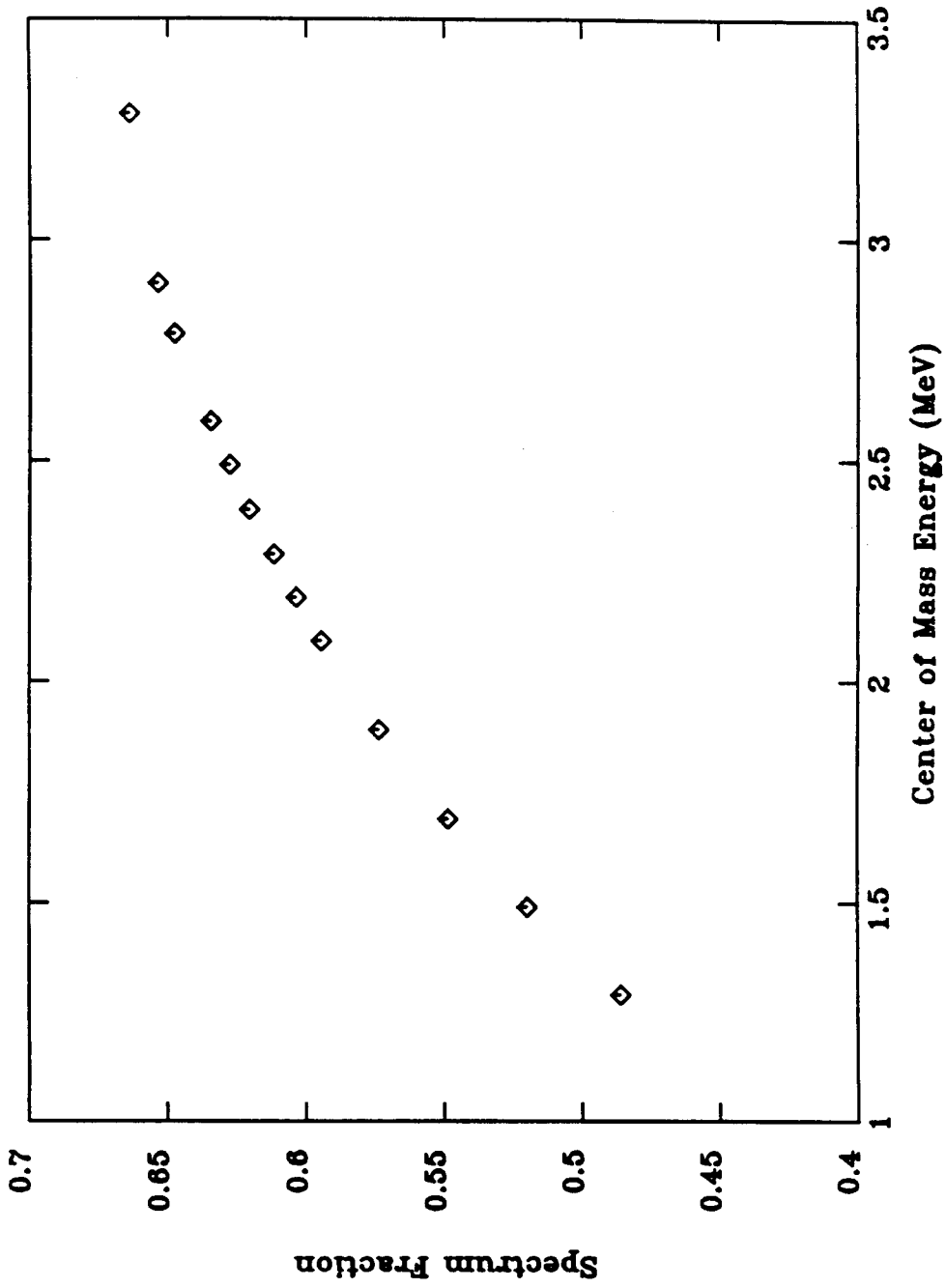
Spectrum Fraction
0.7
0.65
0.6
0.55
0.5
0.45
0.4
1
1.5
2
2.5
3
3.5
Center of Mass Energy (MeV)

Figure 15

SI Calibration

Silicon surface barrier detector calibration data. The data were generated by cross-calibrating the SI detector yield to the calorimeter. The curve through the data is to guide the eye. The two features visible are due to nuclear resonances at E_{cm} = 2.4 MeV and 3.1 MeV. The general upward trend at higher energies is due to the decreasing Rutherford scattering cross-section ($\sigma \propto E^{-2}$). No feature is evident corresponding to the $J^{\pi} = 2^{+}$ resonance at E_{cm} = 2.68 MeV as has been observed previously (KE82).

Figure 15

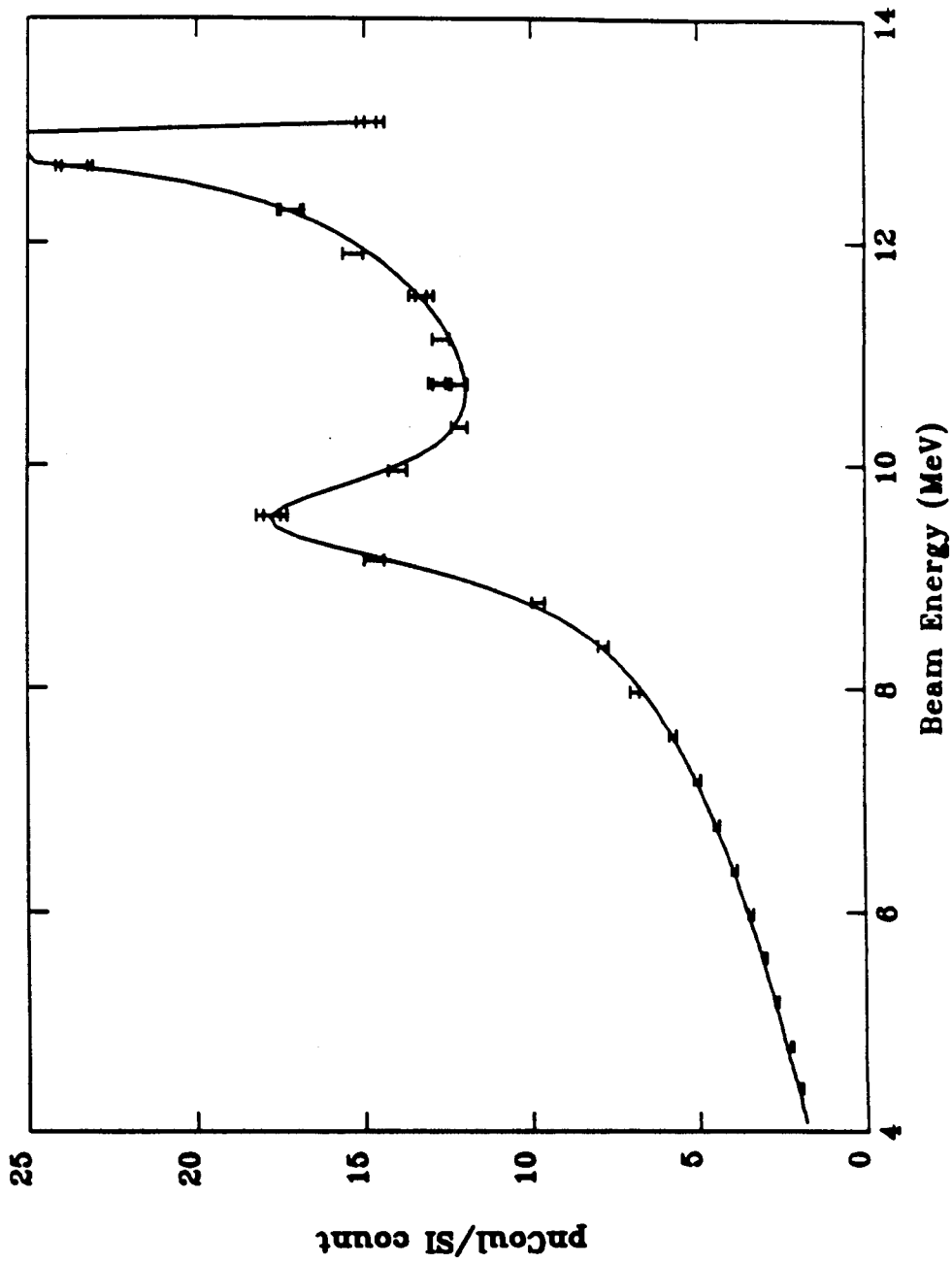

Figure 16

Charge States

Measured charge state fraction as a function of oxygen velocity. These are the values used in the analysis of the present data.

The curve through the data are three parameter fits to a gaussian. Each charge state is fit separately.

Figure 16

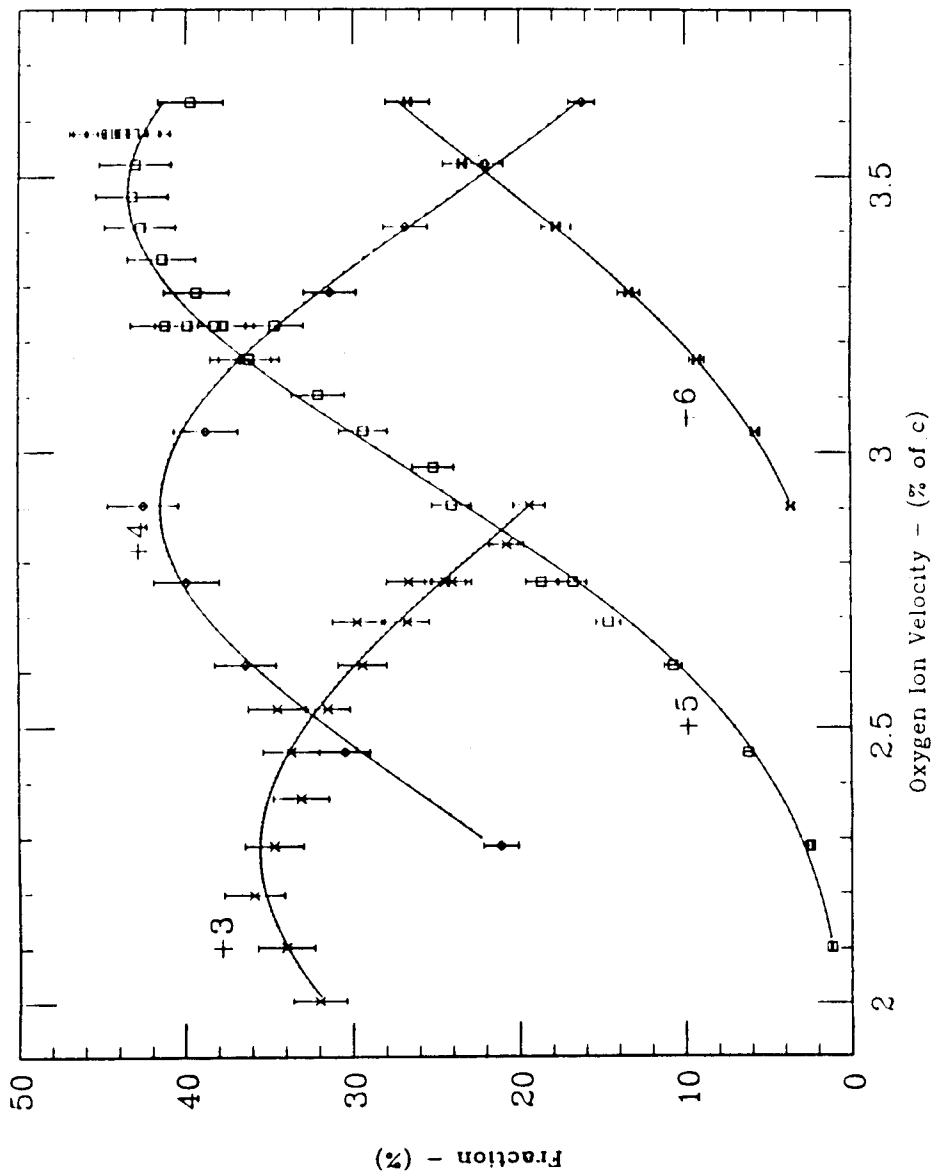

Figure 17

Target Pressure Profile

Target density profile as a function of position along the target. The size of the error bar is represented by the size of the dot.

This demonstrates that more than 97% of the target is contained inside the target can.

Figure 17

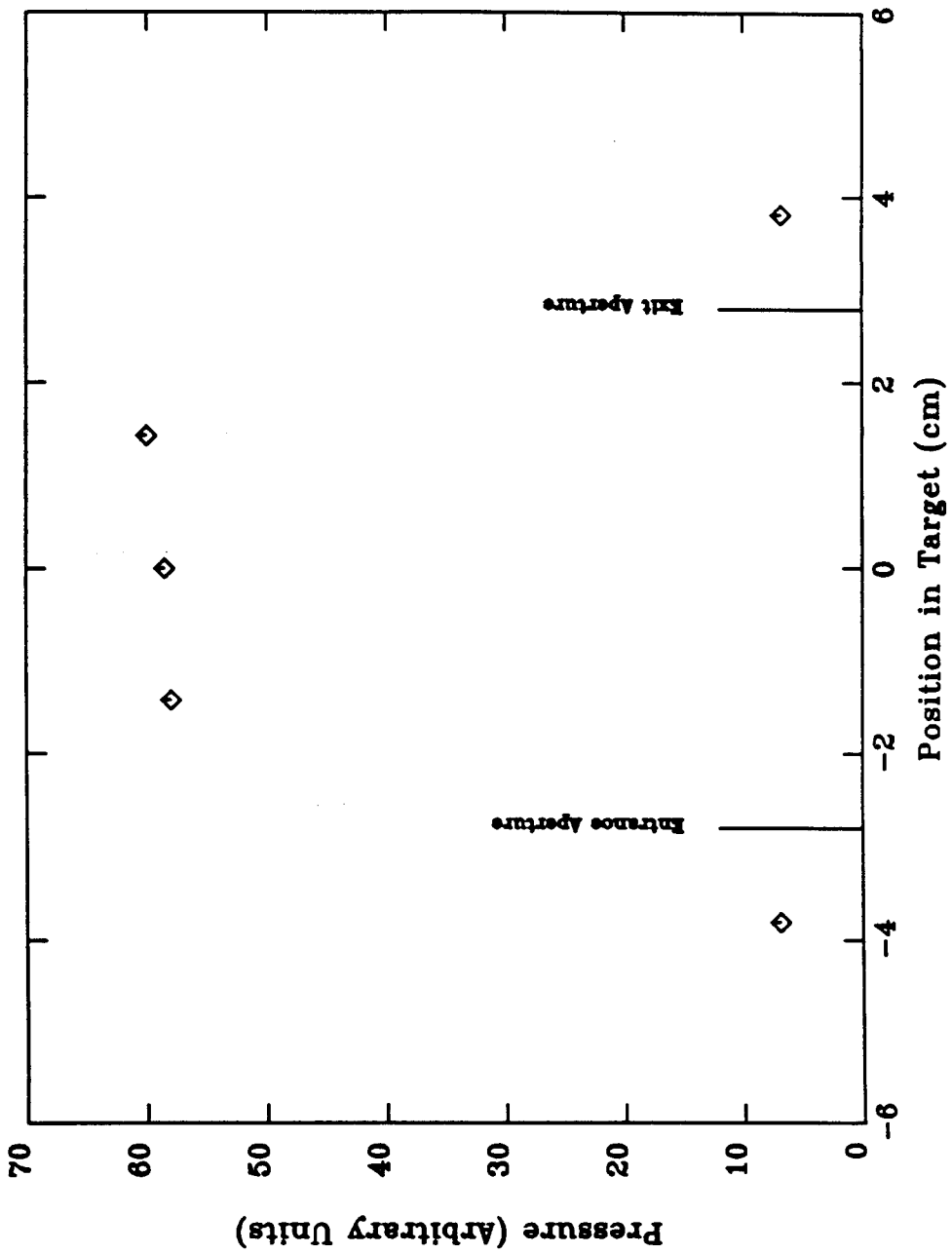
Pressure (Arbitrary Units)
70
60
50
40
30
20
10
0
Position in Target (cm)
6
4
2
0
-2
-4
-6
Exit Aperture
Entrance Aperture

Figure 18

TAC Spectra

Characteristic time of flight spectra for 4 energies. The varying position of the peak is due to the recoil ions taking longer to reach the particle detector at lower energies. The units on the verticle scale on each plot are number of counts, the horizontal scales are arbitrary units that are linear in time. Note the increasing noise level at low energies.

Figure 18

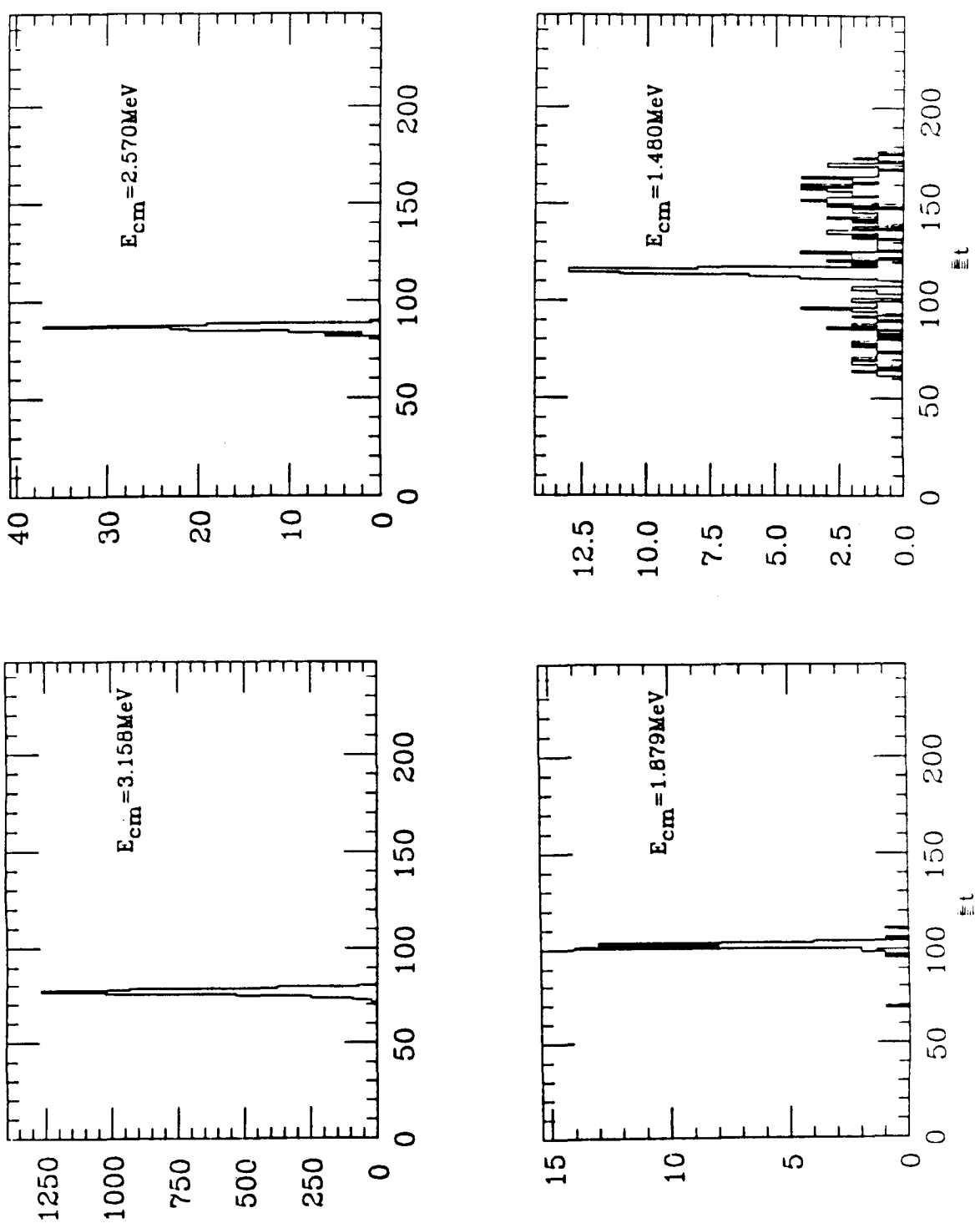

Figure 19

$\varepsilon_{\gamma t}(E\ell)$ Values

The beam transport efficiencies versus center of mass beam energy as described in the text. These are the values determined with a Monte Carlo calculation. The diamonds represent the E1 values and the squares are the E2 values. The discontinuity in the data at about 2 MeV is due to the fact that the selected charge state was switched. Above 2 MeV the 5^+ charge state was selected. Below 2 MeV the 3^+ charge state was chosen. The lines were drawn to guide the eye.

The point at about 2.4 MeV was acquired at Wien filter fields significantly weaker than those that were maintained for all other data points and the transport efficiency is correspondingly higher. Since this variation in the transport efficiency is not seen in the cross-section the conclusion may be drawn that the Monte Carlo calculation properly accounts for variations in the Wien filter fields.

Figure 19

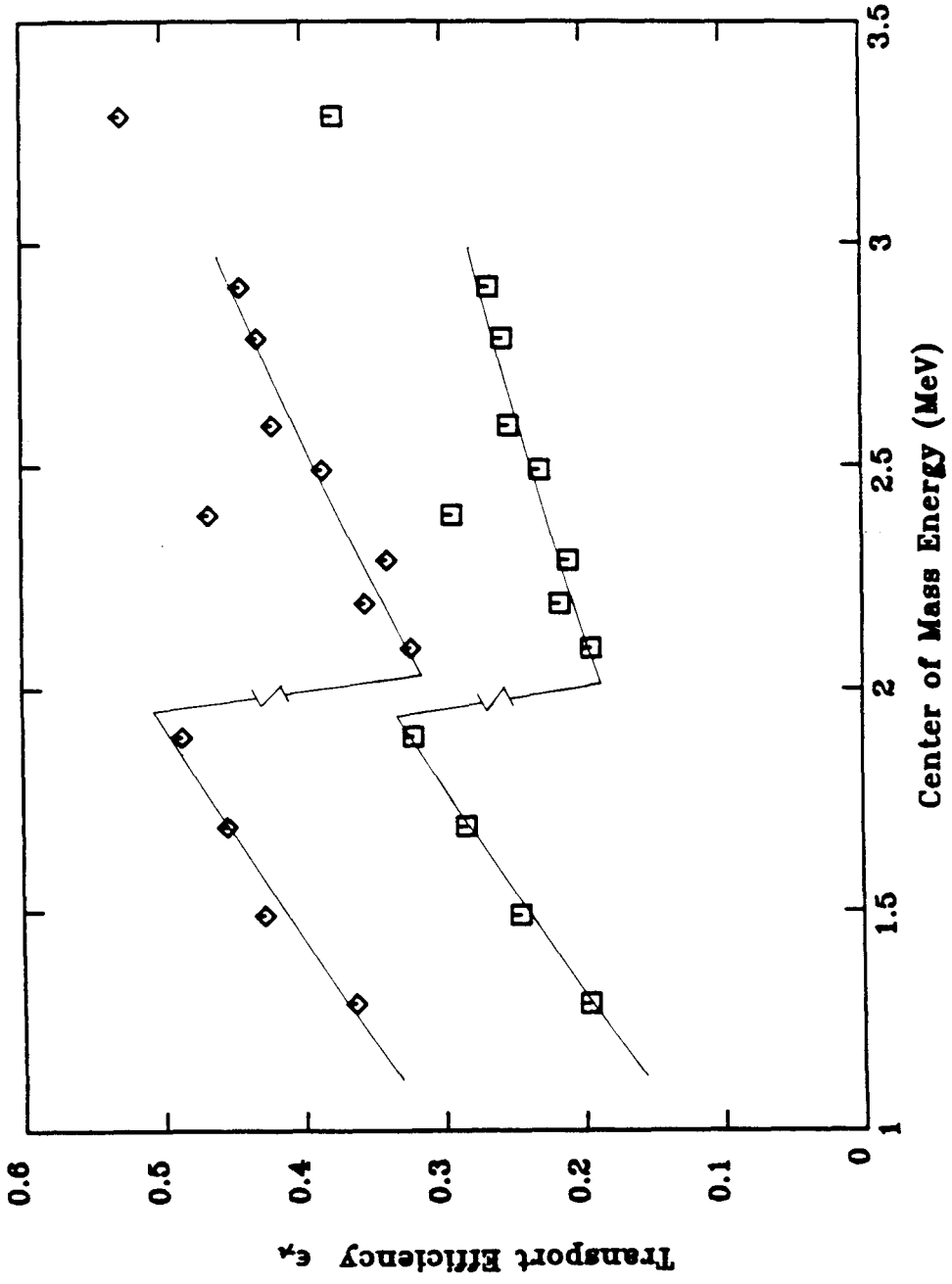
Transport Efficiency ε_A
0.6
0.5
0.4
0.3
0.2
0.1
0
1
1.5
2
2.5
3
3.5
Center of Mass Energy (MeV)

Figure 20

$\sigma(E2)/\sigma(E1)$ Ratios

Values of the E2/E1 cross-section ratios used in the analysis. The dashed line represent the fit due to Funck et al. (FU85), the dotted line is Langanke and Koonin's fit to Dyer and Barnes' (LA83) data, and the solid line is extracted from the experiments of Redder et al. (RE87).

Figure 20

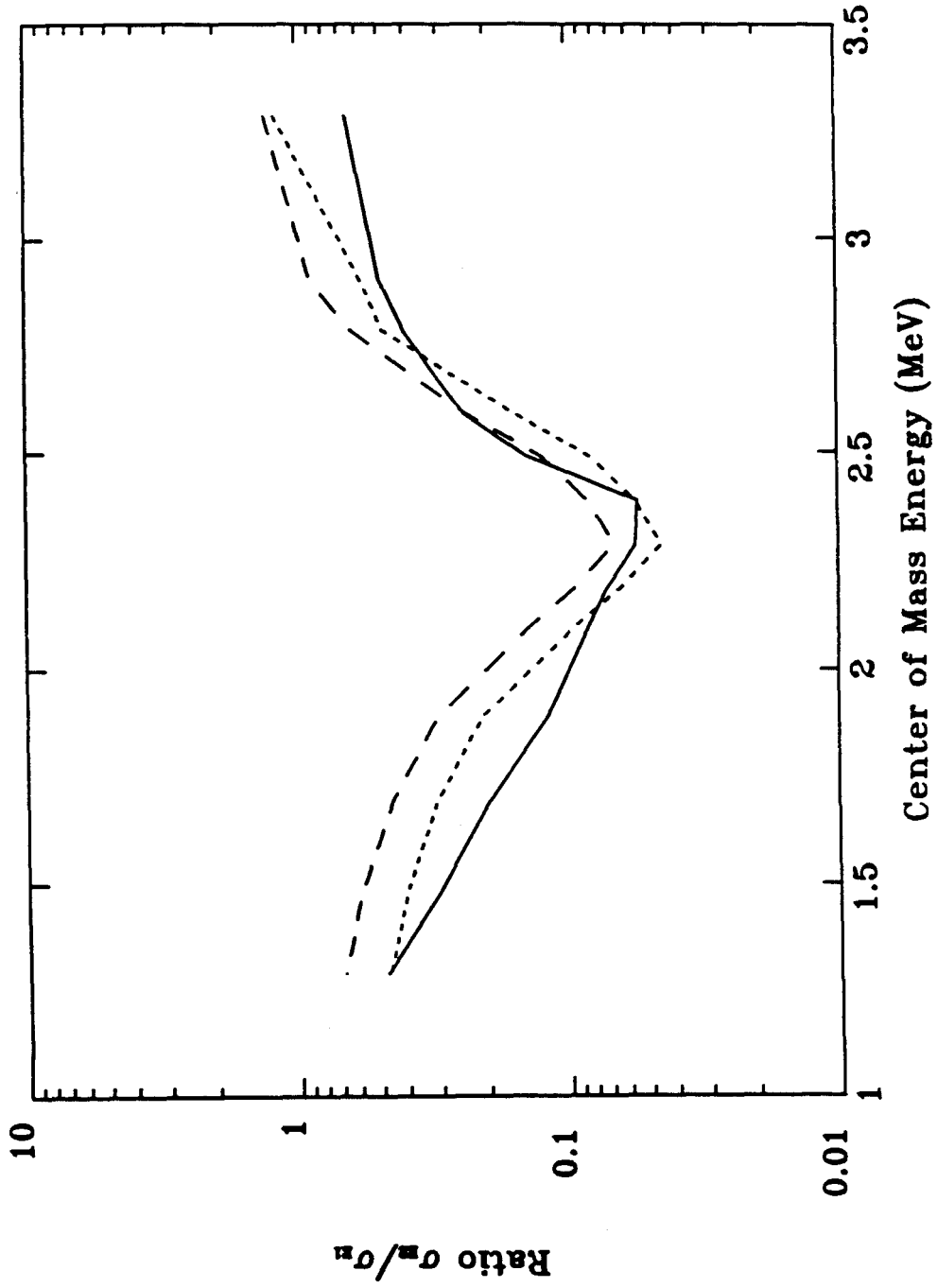
Ratio σ_m/σ_n
10
1
0.1
0.01
1
1.5
2
2.5
3
3.5
Center of Mass Energy (MeV)

Figure 21

E1 Cross-Section

Cross-section (σ(E1)) for $^{12}C(\alpha,\gamma_0)^{16}O$ as a function of center of mass energy.

Figure 21

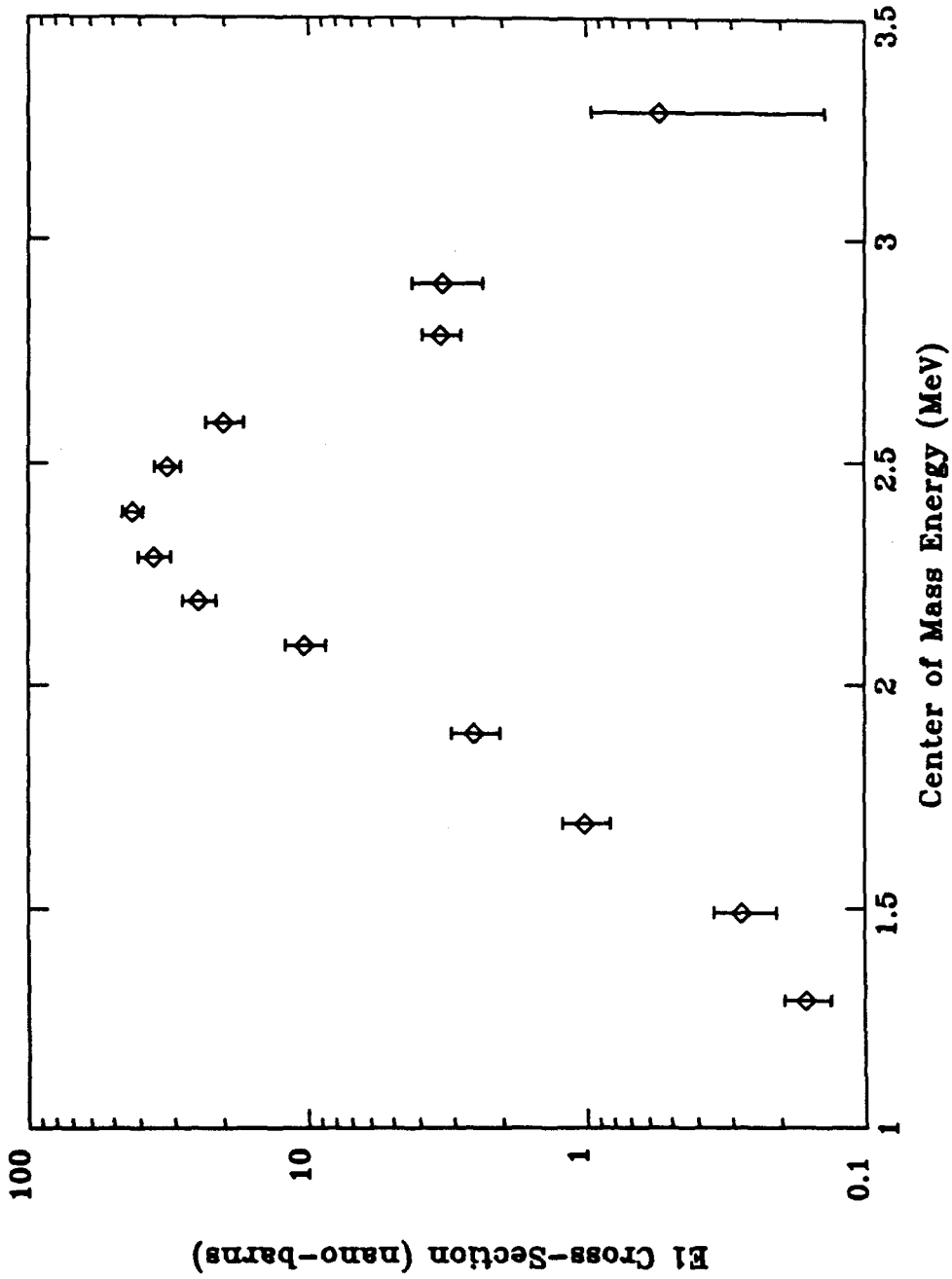
E1 Cross-Section (nano-barns)
100
10
1
0.1
1
1.5
2
2.5
3
3.5
Center of Mass Energy (MeV)

Figure 22

$\sigma_{\gamma_C}/\sigma_{\gamma_O}$ Ratio

Cascade cross-section divided by the ground cross-section for our data. This indicates that the cascade reaction also has some resonance structure in the region of the 1^- resonance.

Figure 22

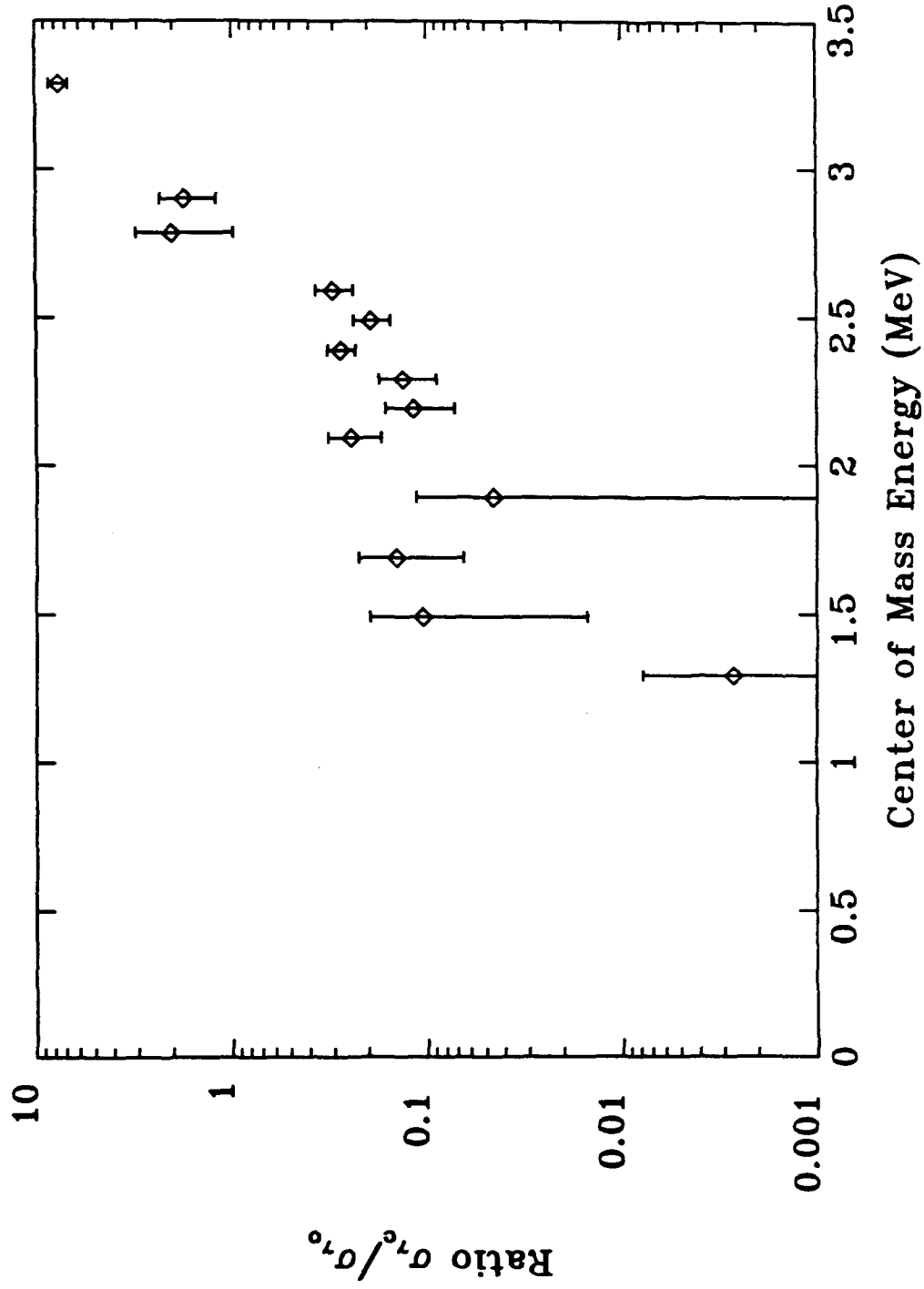
Ratio $\sigma_{\gamma_c}/\sigma_{\gamma_o}$
10
1
0.1
0.01
0.001
0
0.5
1
1.5
2
2.5
3
3.5
Center of Mass Energy (MeV)

Figure 23

2^+ Singles Excitation Function

Excitation function for the $J^\pi = 2^+$ state at $E_x = 9.845$ MeV in $^{12}C(\alpha,\gamma)^{16}O$. The curve is the best-fit to a Breit-Wigner resonance shape. The fit parameters are as follows:

Target Thickness = 26.3 keV,

Resonance width (lab) = 2.367 keV,

Amplitude = 3.00 detected events/ μCoul of beam.

The curve above the data is the excitation function that one obtains if the target thickness is increased to 1 MeV (essentially infinite thickness).

The units on the axes are detected events per μCoul of beam versus lab energy of the ^{12}C beam in MeV.

Figure 23

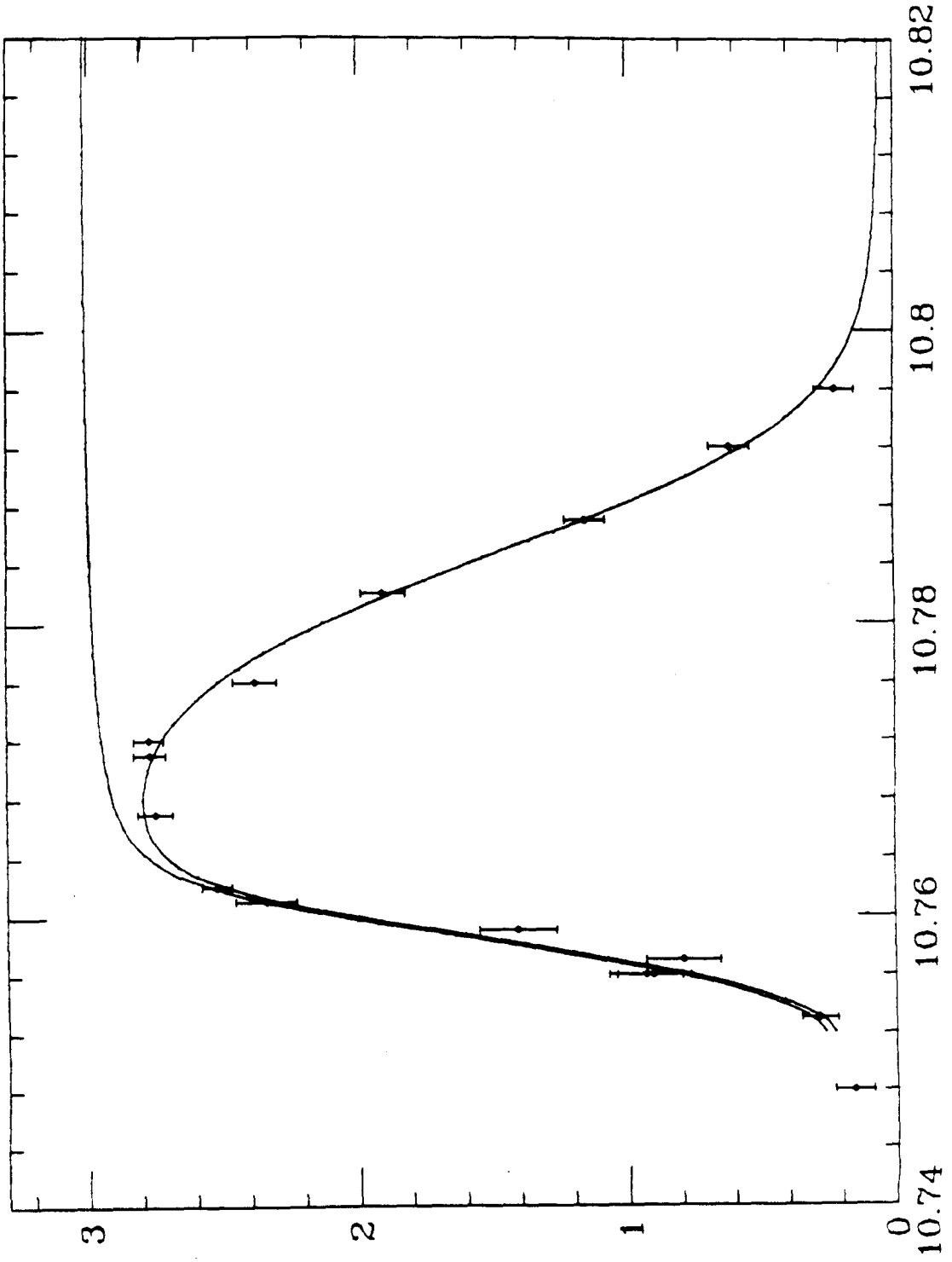

Figure 24

E1 S-Factor

E1 S-factor and extrapolation for the current experiment. The fit parameters are described in the text.

Figure 24

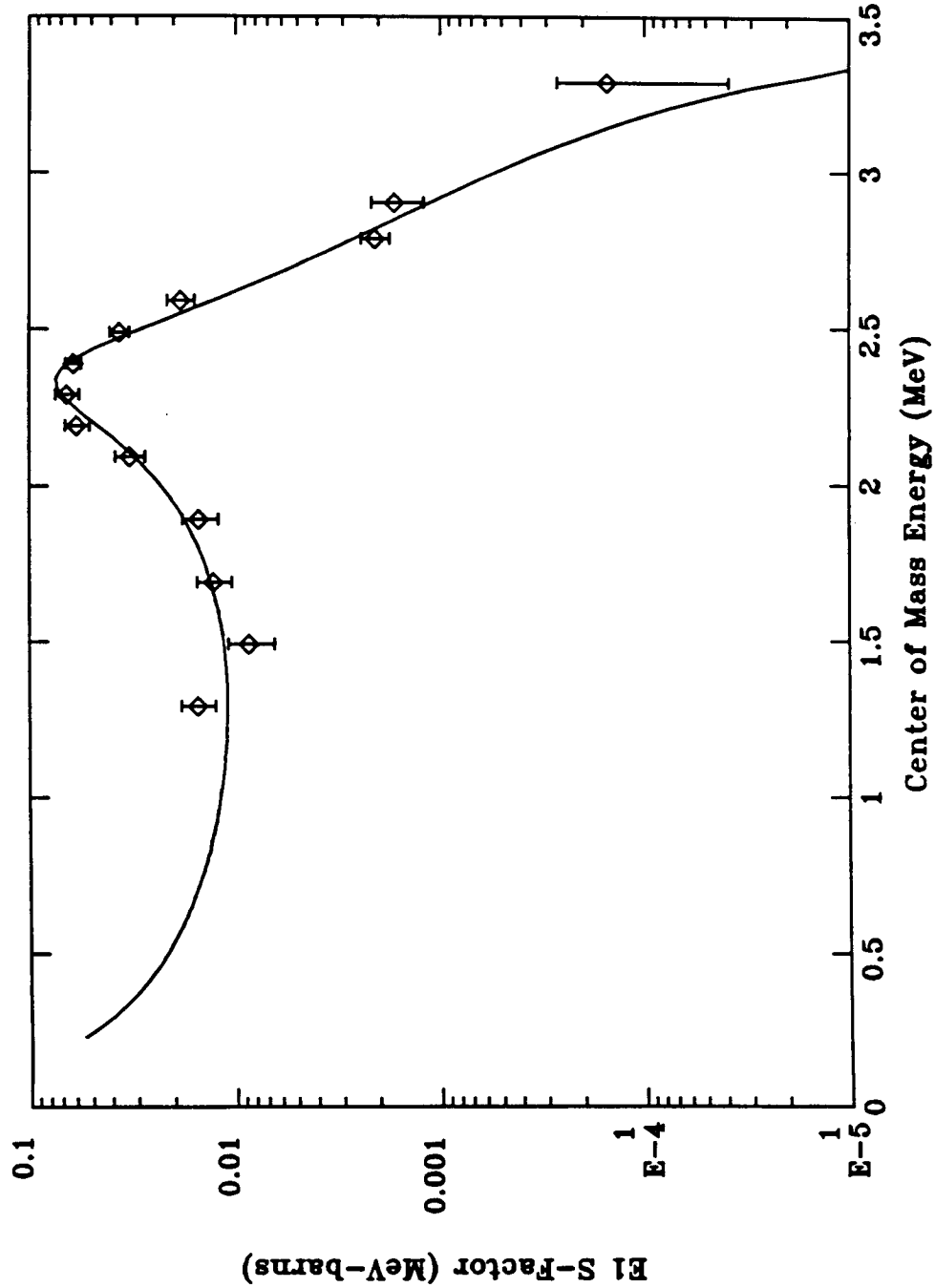
E1 S-Factor (MeV-barns)
0.1
0.01
0.001
1
E-4
1
E-5
0
0.5
1
1.5
2
2.5
3
3.5
Center of Mass Energy (MeV)

Figure 25

E1 S-Factor Comparison

Comparison of the present experimental data and extrapolation to previous E1 S-Factor data (DY74,RE87). The diamonds are the present experiment, the squares are Redder et al., and the xs are Dyer and Barnes' data.

Figure 25

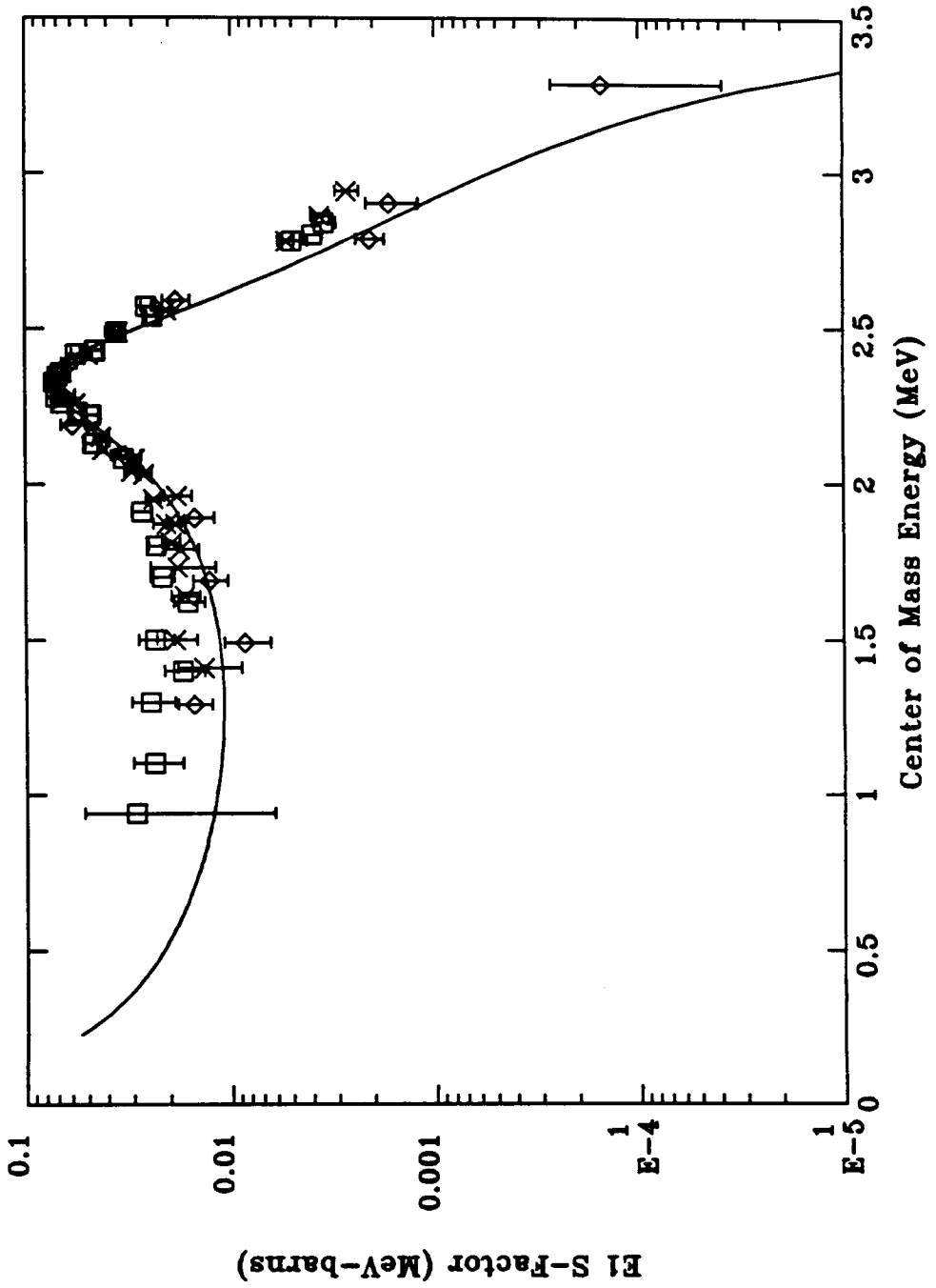
E1 S-Factor (MeV-barns)
0.1
0.01
0.001
1
E-4
1
E-5
0
0.5
1
1.5
2
2.5
3
3.5
Center of Mass Energy (MeV)

Figure A-1

4^+ Cascade Spectrum Fraction

Measured and calculated spectrum fraction for the $J^\pi = 4^+$ resonance.

Figure A-1

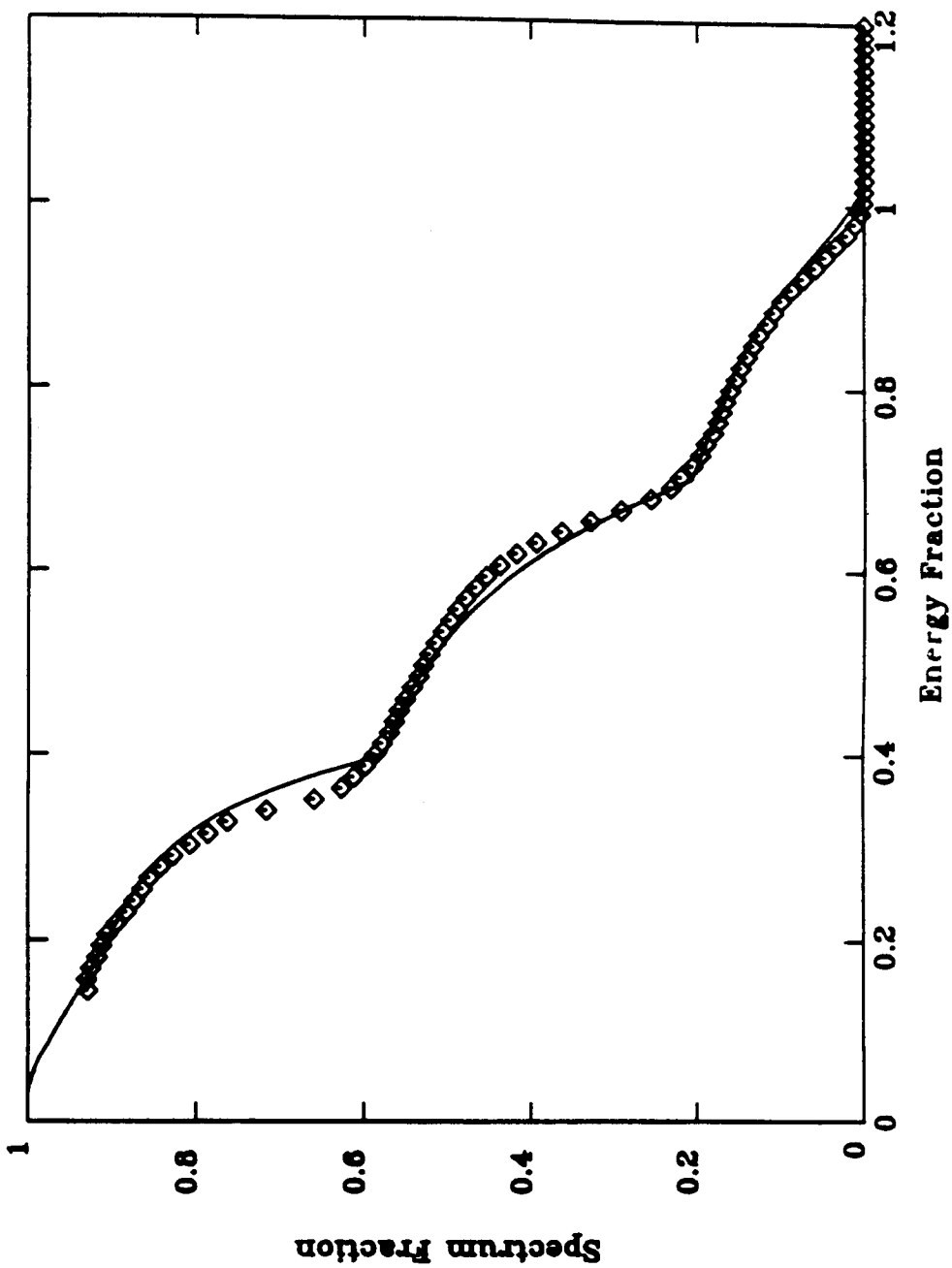
Spectrum Fraction
1
0.8
0.6
0.4
0.2
0
Energy Fraction
0
0.2
0.4
0.6
0.8
1
1.2

Figure B-1

Yield Extrapolation

Yield for 1, 2, 3, and 4 crystals, and the extrapolation to zero crystals. The extrapolation is unambiguous and gives the Y_0 yield at all energies. Graph A shows a large slope because of the large contribution from the cascade reaction at that energy.

Figure B-1

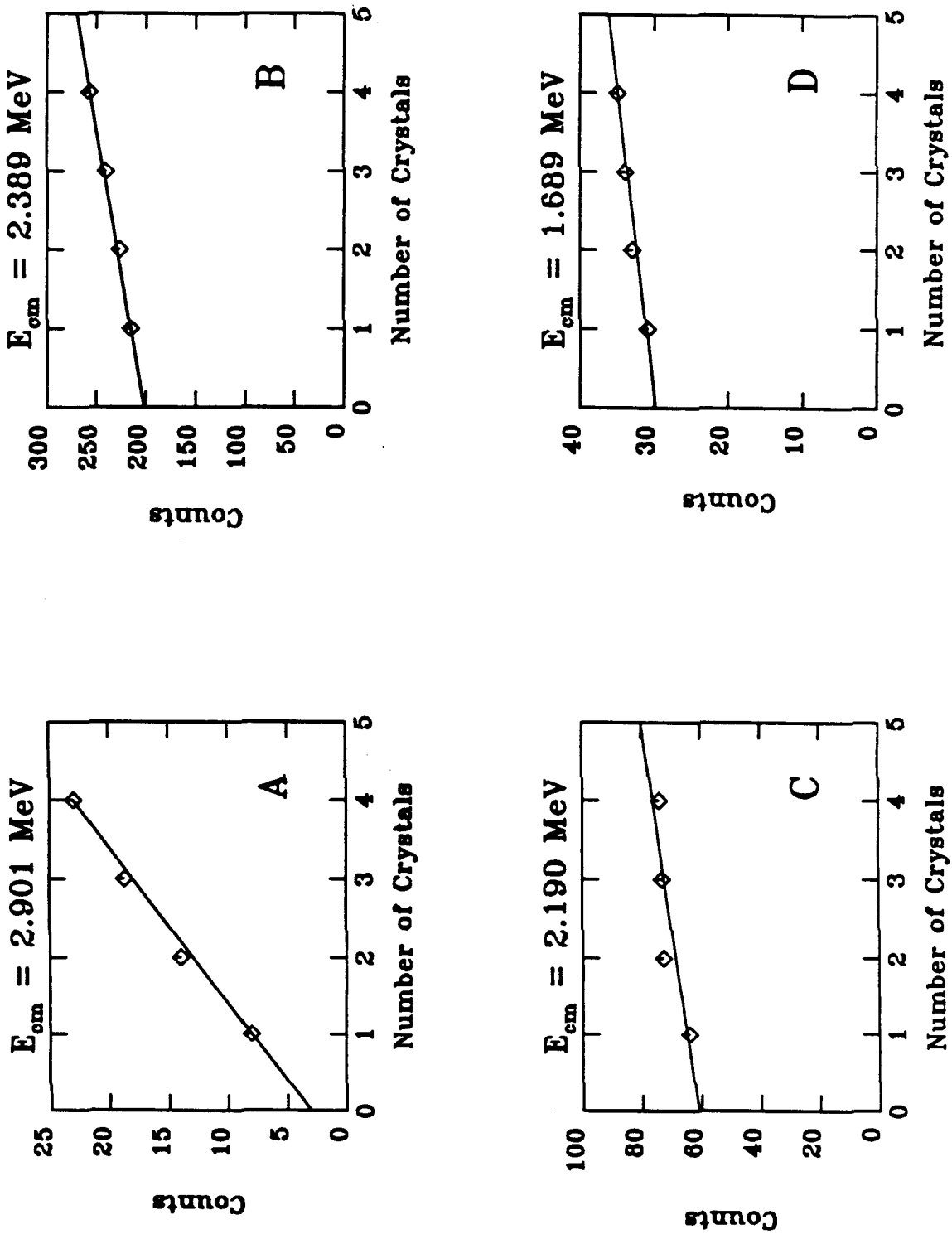
A
E_{cm} = 2.901 MeV
B
E_{cm} = 2.389 MeV
C
E_{cm} = 2.190 MeV
D
E_{cm} = 1.689 MeV
Counts
Number of Crystals

Figure C-1

Example Parameter Space

Possible types of contours for $\chi^2 = \chi^2_{min} + 1$. Part A shows a simple case of independent parameters. That is, the manifold is locally symmetric about the minimum point. Part B shows a case of dependent parameters. For a fixed value of parameter 1, the value of parameter 2 that minimizes χ^2 is not the best fit value.

Figure C-1

A.

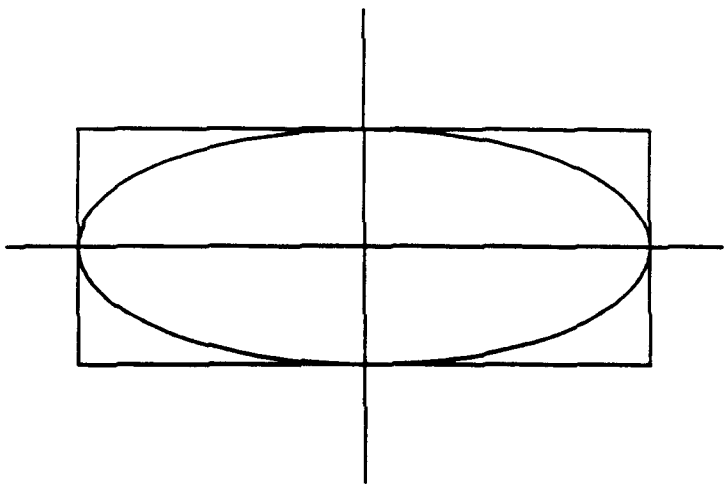

B.

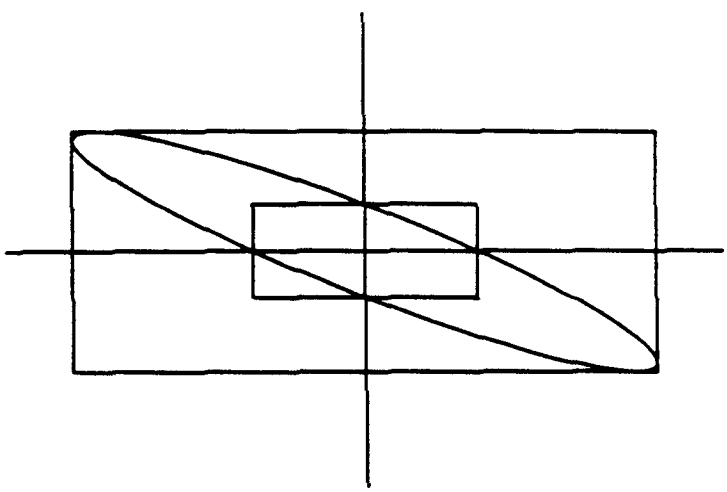

Figure C-2

Sample Histograms

Histograms of S_{E1}(300 keV) values calculated for different assumptions about the errors on the parameters.

ɔh A shows histogram #1 as described in the text. Graph B is histogram #2 and graph C is histogram #3. Graph D shows the distribution of S_{E1}(300 keV) values obtained if the errors on the parameters are taken to be those described in Appendix C, method 1.

The upper right (histogram #2) is the result chosen to best represent the estimated errors on the extrapolation.

Figure C-2

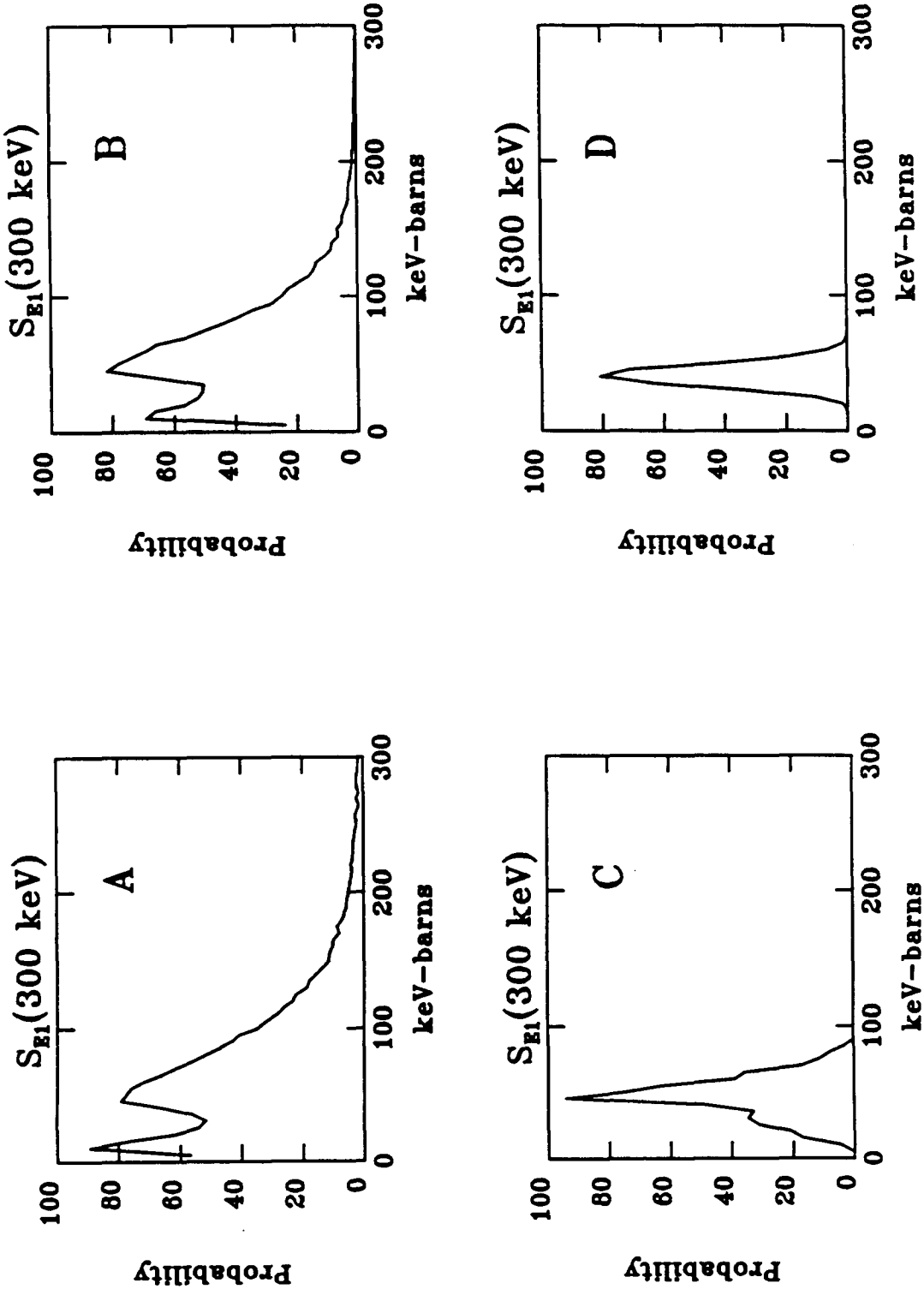
A
B
C
D
S_{E1}(300 keV)
Probability
keV-barns
0
20
40
60
80
100
200
300